Journal of Computational Physics **152,** 687–735 (1999)
Article ID jcph.1999.6256, available online at http://www.idealibrary.com on IDEAL®

Tests of Spurious Transport in Smoothed Particle Hydrodynamics

James C. Lombardi, Jr.,*[,1] Alison Sills,†[,2] Frederic A. Rasio,‡ and Stuart L. Shapiro§

*Department of Astronomy and Center for Radiophysics and Space Research, Cornell University, Ithaca, New York 14853; †Department of Astronomy, Yale University, P.O. Box 208101, New Haven, Connecticut 06520; ‡Department of Physics, Massachusetts Institute of Technology, 6-201, Cambridge, Massachusetts 02139; §Departments of Physics and Astronomy and National Center for Supercomputing Applications, University of Illinois at Urbana Champaign, 1110 West Green Street, Urbana, Illinois 61801
E-mail: lombardi@vassar.edu, asills@astronomy.ohio-state.edu, rasio@mit.edu, shapiro@astro.physics.uiuc.edu

Received July 24, 1998; revised February 16, 1999

We have performed a series of systematic tests to evaluate quantitatively the effects of spurious transport in three-dimensional smoothed particle hydrodynamics (SPH) calculations. Our tests investigate (i) particle diffusion, (ii) shock heating, (iii) numerical viscosity, and (iv) angular momentum transport. The effects of various program parameters on spurious mixing and on viscosity are investigated. The results are useful for quantifying the accuracy of the SPH scheme, especially for problems where shear flows or shocks are present, as well as for problems where true hydrodynamic mixing is relevant. In particular, the particle diffusion coefficients we measure can be used to help estimate the spurious fluid mixing in SPH applications. We examine the different forms of artificial viscosity (AV) which have been proposed by Monaghan, by Hernquist and Katz, and by Balsara. Our tests suggest a single set of values for the AV parameters which are appropriate in a large number of situations: $\alpha \approx 0.5$, $\beta \approx 1$ for the classical AV of Monaghan, $\alpha \approx \beta \approx 0.5$ for the Hernquist and Katz AV, and $\alpha \approx \beta \approx \gamma/2$ for the Balsara AV (where γ is the adiabatic index). We also discuss how these choices should be modified depending on the goals of the particular application. For instance, if spurious particle mixing is not a concern and only weak shocks (Mach number $\mathcal{M} \lesssim 2$) are expected during a calculation, then a smaller value of α is appropriate. Somewhat larger values for α and β may be preferable if an accurate treatment of high Mach number shocks ($\mathcal{M} \gtrsim 10$) is required. We find that both the Hernquist and Katz and Balsara forms introduce only small amounts of numerical viscosity. Furthermore, both Monaghan's and Balsara's AV do well at

[1] Current address: Vassar College, 124 Raymond Avenue, Mail Drop 562, Poughkeepsie, NY 12604-0562.
[2] Current address: Department of Astronomy, The Ohio State University, 174 West 18th Avenue, Columbus, OH 43210.

0021-9991/99 $30.00

treating shocks and at limiting the amount of spurious mixing. For these reasons, we endorse the Balsara AV for use in a broad range of applications.

1. INTRODUCTION

Smoothed particle hydrodynamics (SPH) is a Lagrangian method introduced specifically to deal with astrophysical problems involving self-gravitating fluids moving freely in three dimensions. Pressure-gradient forces are calculated by kernel estimation, directly from the particle positions, rather than by finite differencing on a grid as in other particle methods such as PIC (the particle-in-cell method; see, e.g., [1]) or grid-based methods like PPM (the piecewise parabolic method; see, e.g., [2]). SPH was originally introduced by Lucy [3] and Gingold and Monaghan [4], who applied it to the calculation of dynamical fission instabilities in rapidly rotating stars. Since then, a wide variety of astrophysical fluid dynamics problems have been tackled using SPH (see [5, 6] for reviews). In recent years, these have included planet and star formation [7–9], solar system formation [10], supernova explosions [11, 12], tidal disruption of stars by massive black holes [13], large-scale cosmological structure formation [14, 15], galaxy formation [16, 17], stellar collisions [18, 19], and binary coalescence [20–25]. The SPH method itself has also undergone major advances. Most notably, artificial viscosity (AV) has been incorporated [26–30], as well as powerful algorithms for the calculation of self-gravity including particle-mesh methods [31] and tree algorithms [32, 27, 33].

We have performed systematic tests of the SPH method. We examine the effects of varying a number of SPH-specific parameters and schemes, including the AV parameters, the number of neighbors N_N, the choice of evolution equation (energy vs entropy), and the type of advection algorithm. We concentrate on the examination of spurious transport, including the motion of SPH particles introduced as a numerical artifact of the SPH scheme. Many applications require a careful tracing of particle positions, and in these cases it is essential that the spurious diffusion of SPH particles is small. For example, SPH calculations can be used to establish the amount of composition mixing during stellar collisions [34, 18, 19], which is of primary importance in determining the subsequent stellar evolution of the merger remnant (see, e.g., [35]). In Section 3, we measure particle diffusion coefficients which allow one to estimate the extent of spurious fluid mixing in SPH applications. In Section 4, we then apply these diffusion coefficients to a simple self-gravitating system.

We present a comparison of three different AV forms, namely those of Monaghan [28], Hernquist and Katz [27], and Balsara [29]. The tests performed include a version of the Riemann shock-tube problem with periodic boundary conditions (Section 5). We also study and measure numerical viscosity, both in the context of a pure shear flow constructed in a periodic box with slipping boundary conditions (Subsection 6.1), and in a rapidly, differentially rotating, self-gravitating system (Subsection 6.2). Numerical viscosity is important since it causes the spurious exchange of momentum and angular momentum among shear layers. For each of the AV forms, we investigate how the AV parameters can be adjusted to achieve an accurate description of shocks, while still controlling spurious mixing and shear viscosity. It is the tests of Sections 5 and 6 upon which we base our comparison of the various AV forms.

All of our results are summarized and discussed in Section 7. Other tests of SPH include those by Hernquist and Katz [27] and Steinmetz and Müller [36]. In addition, comparisons

between SPH and Eulerian codes have been presented in the literature in a variety of contexts: stellar collisions [37], cosmology [38], rotating stars [39], coalescing neutron stars [40], circumstellar disks [9], and shock-tube tests [30].

2. NUMERICAL METHOD

Many different implementations of SPH exist (e.g., [31, 27, 41]), and in this section we give a brief description of the more popular schemes.

2.1. *Density, Pressure, and Entropy*

An SPH particle can be thought of as a Lagrangian fluid element. Associated with particle i is its position $\mathbf{r}_i$, velocity $\mathbf{v}_i$, and mass m_i. In addition, each particle carries SPH-specific parameters including a purely numerical "smoothing length" h_i, specifying the local spatial resolution. An estimate of the fluid density at $\mathbf{r}_i$ is calculated from the masses, positions, and smoothing lengths of neighboring particles as a local weighted average,

$$\rho_i = \sum_j m_j W_{ij}, \tag{1}$$

where the symmetric weights $W_{ij} = W_{ji}$ can be calculated from the method of Hernquist and Katz [27], as

$$W_{ij} = \frac{1}{2}[W(|\mathbf{r}_i - \mathbf{r}_j|, h_i) + W(|\mathbf{r}_i - \mathbf{r}_j|, h_j)]. \tag{2}$$

Here $W(r, h)$ is a smoothing (or interpolation) kernel, for which we use the second-order accurate form of Monaghan and Lattanzio [41],

$$W(r,h) = \frac{1}{\pi h^3} \begin{cases} 1 - \frac{3}{2}\left(\frac{r}{h}\right)^2 + \frac{3}{4}\left(\frac{r}{h}\right)^3, & 0 \le \frac{r}{h} < 1, \\ \frac{1}{4}\left[2 - \left(\frac{r}{h}\right)\right]^3, & 1 \le \frac{r}{h} < 2, \\ 0, & \frac{r}{h} \ge 2. \end{cases} \tag{3}$$

Depending on which evolution equation is integrated (see Eqs. (20) and (21) below), particle i also carries either the parameter u_i, the local internal energy per unit mass, or A_i, the entropy variable, a function of the local specific entropy. Arbitrary equations of state (e.g., adiabatic, isothermal, even equations of state for metals and rocky materials; cf. [42]) are permitted in SPH. The calculations presented in this paper use, unless otherwise noted, polytropic equations of state with $\gamma = 5/3$, appropriate for an ideal monatomic gas. The pressure at $\mathbf{r}_i$ is therefore calculated either as

$$p_i = (\gamma - 1)\rho_i u_i, \tag{4}$$

or

$$p_i = A_i \rho_i^{\gamma}. \tag{5}$$

We define the specific entropy of particle i to be

$$s_i \equiv \frac{1}{\gamma - 1} \ln\left(\frac{p_i}{\rho_i^{\gamma}(\gamma - 1)}\right), \tag{6}$$

and the total entropy of the system $S = \sum_i m_i s_i$. Equation (6) is a definition of convenience: we refer to the quantity s_i as entropy, even though it differs from the true thermodynamic entropy (which depends on the composition of the fluid being represented). Although both s_i and the true thermodynamic entropy are conserved in adiabatic processes, it is s_i which arises naturally when studying the dynamical stability of self-gravitating fluids.

2.2. *Dynamic Equations and Gravity*

Particle positions are updated either by

$$\dot{\mathbf{r}}_i = \mathbf{v}_i, \tag{7}$$

or the more general XSPH method

$$\dot{\mathbf{r}}_i = \mathbf{v}_i + \epsilon \sum_j m_j \frac{\mathbf{v}_j - \mathbf{v}_i}{\rho_{ij}} W_{ij}, \tag{8}$$

where $\rho_{ij} = (\rho_i + \rho_j)/2$ and ϵ is a constant parameter in the range $0 < \epsilon < 1$ [28]. Equation (8), as compared to Eq. (7), changes particle positions at a rate closer to the local smoothed velocity. The XSPH method was originally proposed as a means of decreasing spurious interparticle penetration across the interface of two colliding fluids.

The velocity of particle i is updated according to

$$\dot{\mathbf{v}}_i = \mathbf{a}_i^{(\mathrm{Grav})} + \mathbf{a}_i^{(\mathrm{SPH})}, \tag{9}$$

where $\mathbf{a}_i^{(\mathrm{Grav})}$ is the gravitational acceleration and

$$\mathbf{a}_i^{(\mathrm{SPH})} = -\sum_j m_j \left[\left(\frac{p_i}{\rho_i^2} + \frac{p_j}{\rho_j^2}\right) + \Pi_{ij}\right] \boldsymbol{\nabla}_i W_{ij}. \tag{10}$$

The AV term Π_{ij} (see Subsection 2.3) ensures that correct jump conditions are satisfied across (smoothed) shock fronts, while the rest of Eq. (10) represents one of many possible SPH-estimators for the acceleration due to the local pressure gradient (see, e.g., [43]).

To provide reasonable accuracy, an SPH code must solve the equations of motion of a large number of particles (typically $N \gg 1000$). This rules out a direct summation method for calculating the gravitational field of the system, unless special purpose hardware such as GRAPE is used [17, 44]. In most implementations of SPH, particle-mesh algorithms [31, 20, 45] or tree-based algorithms [27, 46] are used to calculate the gravitational accelerations $\mathbf{a}_i^{(\mathrm{Grav})}$. Tree-based algorithms perform better for problems involving large dynamic ranges in density, such as star formation and large-scale cosmological calculations. For problems such as stellar interactions, where density contrasts rarely exceed a factor $\sim 10^2 - 10^3$, grid-based algorithms and direct solvers are generally faster. Tree-based and grid-based algorithms are also used to calculate lists of nearest neighbors for each particle exactly as in gravitational N-body calculations (see, e.g., [1, 47]).

Our SPH codes are slightly modified versions of codes originally developed by Rasio [48], with implementations similar to those adopted by Hernquist and Katz [27]. Our 3D code has the option of including gravity and calculates the gravitational field by a particle-mesh convolution algorithm which uses a grid-based FFT solver [1, 49]. More specifically, the smoothed density sets the values of the source term for Poisson's equation at grid points. The FFT-based convolution algorithm then solves for the gravitational potential on that grid. Forces at grid points are obtained by finite differencing, and then interpolated onto the particle positions. We have found that, for our tests involving self-gravitating fluids, it is relatively easy to make the gravity accurate enough that it is not a significant source of error. Therefore, the results of this paper can be applied to any SPH code regardless of its gravitational scheme.

2.3. *Artificial Viscosity*

We now present three commonly used AV forms which are tested in this paper. In Subsections 7.2 and 7.3 we will discuss the results of these tests, while in Subsection 7.4 we discuss which of the AV forms performs best in which circumstances.

A symmetrized version of the AV form proposed by Monaghan [28] is often adopted,

$$\Pi_{ij} = \frac{-\alpha \mu_{ij} c_{ij} + \beta \mu_{ij}^2}{\rho_{ij}}, \tag{11}$$

where α and β are constant parameters, $c_{ij} = (c_i + c_j)/2$ (with $c_i = (\gamma p_i/\rho_i)^{1/2}$ being the speed of sound in the fluid at $\mathbf{r}_i$), and

$$\mu_{ij} = \begin{cases} \frac{(\mathbf{v}_i - \mathbf{v}_j)\cdot(\mathbf{r}_i - \mathbf{r}_j)}{h_{ij}(|\mathbf{r}_i - \mathbf{r}_j|^2/h_{ij}^2 + \eta^2)} & \text{if } (\mathbf{v}_i - \mathbf{v}_j)\cdot(\mathbf{r}_i - \mathbf{r}_j) < 0 \\ 0 & \text{if } (\mathbf{v}_i - \mathbf{v}_j)\cdot(\mathbf{r}_i - \mathbf{r}_j) \geq 0 \end{cases} \tag{12}$$

with $h_{ij} = (h_i + h_j)/2$. We will refer to viscosities of this form as the "classical" AV. This form represents a combination of a bulk viscosity (linear in μ_{ij}) and a von Neumann–Richtmyer viscosity (quadratic in μ_{ij}). The von Neumann–Richtmyer AV was initially introduced to suppress particle interpenetration in the presence of strong shocks. Our tests will demonstrate that, for constant α and β, Eq. (11) performs best when $\alpha \approx 0.5$, $\beta \approx 1$, and $\eta^2 \sim 10^{-2}$, although, as discussed in Subsection 7.4, these choices should be adjusted to fit the particular goals of an application. Morris and Monaghan [30] have recently implemented Eq. (12) with a *time varying* coefficient α, and with $\beta = 2\alpha$.

Another form for the AV, introduced by Hernquist and Katz [27], calculates Π_{ij} directly from the SPH estimate of the divergence of the velocity field,

$$\Pi_{ij} = \begin{cases} \frac{q_i}{\rho_i^2} + \frac{q_j}{\rho_j^2} & \text{if } (\mathbf{v}_i - \mathbf{v}_j)\cdot(\mathbf{r}_i - \mathbf{r}_j) < 0 \\ 0 & \text{if } (\mathbf{v}_i - \mathbf{v}_j)\cdot(\mathbf{r}_i - \mathbf{r}_j) \geq 0, \end{cases} \tag{13}$$

where

$$q_i = \begin{cases} \alpha \rho_i c_i h_i |\nabla \cdot \mathbf{v}|_i + \beta \rho_i h_i^2 |\nabla \cdot \mathbf{v}|_i^2 & \text{if } (\nabla \cdot \mathbf{v})_i < 0 \\ 0 & \text{if } (\nabla \cdot \mathbf{v})_i \geq 0 \end{cases} \tag{14}$$

and

$$(\nabla \cdot \mathbf{v})_i = \frac{1}{\rho_i} \sum_j m_j (\mathbf{v}_j - \mathbf{v}_i) \cdot \nabla_i W_{ij}. \tag{15}$$

We will refer to this form as the HK AV. Although this form provides a slightly less accurate description of shocks than Eq. (11), it does exhibit less shear viscosity. Our tests show that $\alpha \approx \beta \approx 0.5$ is often an appropriate choice for the HK AV (see Subsection 7.4).

More recently, Balsara [29] has proposed the AV form

$$\Pi_{ij} = \left(\frac{p_i}{\rho_i^2} + \frac{p_j}{\rho_j^2} \right) \left(-\alpha \mu_{ij} + \beta \mu_{ij}^2 \right), \tag{16}$$

where

$$\mu_{ij} = \begin{cases} \frac{(\mathbf{v}_i - \mathbf{v}_j) \cdot (\mathbf{r}_i - \mathbf{r}_j)}{h_{ij} (|\mathbf{r}_i - \mathbf{r}_j|^2 / h_{ij}^2 + \eta^2)} \frac{f_i + f_j}{2 c_{ij}} & \text{if } (\mathbf{v}_i - \mathbf{v}_j) \cdot (\mathbf{r}_i - \mathbf{r}_j) < 0 \\ 0 & \text{if } (\mathbf{v}_i - \mathbf{v}_j) \cdot (\mathbf{r}_i - \mathbf{r}_j) \geq 0. \end{cases} \tag{17}$$

Here f_i is the form function for particle i, defined by

$$f_i = \frac{|\nabla \cdot \mathbf{v}|_i}{|\nabla \cdot \mathbf{v}|_i + |\nabla \times \mathbf{v}|_i + \eta' c_i / h_i}, \tag{18}$$

where the factor $\eta' \sim 10^{-4}$–10^{-5} prevents numerical divergences, $(\nabla \cdot \mathbf{v})_i$ is given by Eq. (15), and

$$(\nabla \times \mathbf{v})_i = \frac{1}{\rho_i} \sum_j m_j (\mathbf{v}_i - \mathbf{v}_j) \times \nabla_i W_{ij}. \tag{19}$$

The function f_i acts as a switch, approaching unity in regions of strong compression ($|\nabla \cdot \mathbf{v}|_i \gg |\nabla \times \mathbf{v}|_i$) and vanishing in regions of large vorticity ($|\nabla \times \mathbf{v}|_i \gg |\nabla \cdot \mathbf{v}|_i$). Consequently, this AV has the advantage that it is suppressed in shear layers. Throughout this paper we use $\eta' = 10^{-5}$, a choice which does not significantly affect our results. Note that since $(p_i/\rho_i^2 + p_j/\rho_j^2) \approx 2c_{ij}^2/(\gamma \rho_{ij})$, Eq. (16) resembles Eq. (11) when $|\nabla \cdot \mathbf{v}|_i \gg |\nabla \times \mathbf{v}|_i$, provided one rescales the α and β in Eq. (16) to be a factor of $\gamma/2$ times the α and β in Eq. (11). We will show that $\alpha \approx \beta \approx \gamma/2$ is often an appropriate choice for the Balsara AV.

2.4. *Thermodynamics*

To complete the description of the fluid, either u_i or A_i is evolved according to a discretized version of the first law of thermodynamics,

$$\frac{du_i}{dt} = \frac{1}{2} \sum_j m_j \left(\frac{p_i}{\rho_i^2} + \frac{p_j}{\rho_j^2} + \Pi_{ij} \right) (\mathbf{v}_i - \mathbf{v}_j) \cdot \nabla_i W_{ij}, \tag{20}$$

or

$$\frac{dA_i}{dt} = \frac{\gamma - 1}{2 \rho_i^{\gamma - 1}} \sum_j m_j \, \Pi_{ij} (\mathbf{v}_i - \mathbf{v}_j) \cdot \nabla_i W_{ij}. \tag{21}$$

We call Eq. (20) the "energy equation," while Eq. (21) is the "entropy equation." Which equation one should integrate depends upon the problem being treated. For instance, thermodynamic processes such as heating and cooling [14] and nuclear burning [12] can be incorporated more easily into the energy equation.

The derivations of Eqs. (20) and (21) neglect the time variation of h_i. Therefore if we integrate the energy equation, even in the absence of AV, the total entropy of the system will not be strictly conserved if the particle smoothing lengths are allowed to vary in time; if the entropy equation is used, the total entropy would then be strictly conserved when $\Pi_{ij} = 0$, but not the total energy [48, 50]. For more accurate treatments involving time-dependent smoothing lengths, see Nelson and Papaloizou [51, 52] and Serna *et al.* [53].

There are many other equivalent forms of the basic SPH equations which reduce to the correct fluid equations in the limit $N \to \infty$, $h_i \to 0$. However, most of them will satisfy their associated conservation equations only approximately, i.e., up to errors which tend to zero only in this limit. In contrast, the above equations have the virtue of conserving energy and momentum exactly, independent of the number of particles used, as long as the smoothing lengths are held fixed (e.g., [48]). Of course, in the numerical solution, errors will still be introduced by the time-integration scheme.

2.5. *Integration in Time*

For a stable time integration scheme, the timestep must satisfy a Courant-like condition with h_i replacing the usual grid separation. For accuracy, the timestep must be a small enough fraction of the system's dynamical time. We calculate the timestep as

$$\Delta t = C_N \,\mathrm{Min}(\Delta t_1, \Delta t_2), \tag{22}$$

where the constant dimensionless Courant number C_N typically satisfies $0.1 \lesssim C_N \lesssim 0.8$, where

$$\Delta t_1 = \min_i (h_i / \dot{v}_i)^{1/2}, \tag{23}$$

and where for Δt_2 we use one of two types of expressions, the simplest being

$$\Delta t_2 = \min_i \left(\frac{h_i}{\left(c_i^2 + v_i^2\right)^{1/2}} \right). \tag{24}$$

In the presence of strong shocks, equations such as (24) can allow for fairly large entropy changes in a single timestep when C_N is large. This problem can be eliminated by using smaller C_N, or by adopting a more sophisticated expression introduced by Monaghan [28]:

$$\Delta t_2 = \min_i \left(\frac{h_i}{c_i + 1.2\alpha c_i + 1.2\beta \,\mathrm{Max}_j |\mu_{ij}|} \right). \tag{25}$$

If the Hernquist and Katz AV (Eq. (13)) is used, the quantity $\mathrm{Max}_j|\mu_{ij}|$ in Eq. (25) can be replaced by $h_i|\nabla \cdot \mathbf{v}|_i$ if $(\nabla \cdot \mathbf{v})_i < 0$, and by 0 otherwise. By accounting for AV-induced diffusion, the α and β terms in the denominator of Eq. (25) allow for a more efficient use of computational resources than simply using a smaller value of C_N. In this paper, we will label the timestep routine by an S (for "simple") when we implement Eqs. (22), (23), and (24), and by an M (for Monaghan) when we implement (22), (23), and (25).

The evolution equations are integrated using a second-order explicit leap-frog scheme. Such a low order scheme is appropriate because the dominate source of error for the evolution is the noise in particle interactions due to numerical discreteness effects. Other details of our implementation, as well as a number of test-bed calculations using our SPH code, are presented in Rasio and Shapiro [54, 20].

2.6. *Smoothing Lengths and Accuracy*

The size of the smoothing lengths is often chosen such that particles roughly maintain some predetermined number of neighbors N_N. Typical values of N_N range from about 20 to 100. If a particle interacts with too few neighbors, then the forces on it are sporadic, a poor approximation to the forces on a true fluid element. In general, one finds that, for given physical conditions, the noise level in a calculation always decreases when N_N is increased.

At the other extreme, large neighbor numbers degrade the resolution by requiring unreasonably large smoothing lengths. However, higher accuracy is obtained in SPH calculations only when *both* the number of particles N *and* the number of neighbors N_N are increased, with N increasing faster than N_N so that the smoothing lengths h_i decrease. Otherwise (e.g., if N is increased while maintaining N_N constant) the SPH method is *inconsistent*, i.e., it converges to an unphysical limit [48]. The choice of N_N for a given calculation is therefore dictated by a compromise between an acceptable level of numerical noise and the desired spatial resolution (which is $\approx h \propto 1/N_N^{1/d}$ in d dimensions).

3. SIMPLE BOX TESTS

3.1. *Measuring SPH Particle Diffusion*

Simulations of a homogeneous volume of gas, at rest and in the absence of gravity, provide a natural environment to examine spurious diffusion of SPH particles. In the ideal simulation of a motionless fluid, no SPH particles would move, and the thermodynamic variables would remain constant. However, an SPH system always contains some level of noise, which leads to spurious motion of particles even in the absence of any bulk flow.

In order to model such a system, we introduce periodic boundary conditions in a cubical box, adopting the standard technique of molecular dynamics (cf. [55]): whenever an SPH particle leaves the box, it is reintroduced with the same velocity vector on the opposing face, directly across from where it exited. Particles with smoothing kernels extending beyond a side of the box can have neighbors near the opposing side, once periodicity is taken into account. More precisely, particle j has particle i as a neighbor if there exists integers k, l, and m such that the position $(x_i + kL, y_i + lL, z_i + mL)$ is within a distance $2h_j$ of (x_j, y_j, z_j), where L is the length of the box. This allows particles near a corner of the box to interact with image particles from any of the other seven corners. Unless otherwise noted, the calculations presented in this section employ equal mass particles, all with the same time-independent smoothing length h chosen such that the average number of neighbors N_N is 20, 32, 48, or 64. The total number of particles N in the box is unimportant, as long as it is large enough that surface effects can be neglected. To ensure this, we always choose N such that $L/h \gtrsim 16$.

For the diffusion tests of this section, the natural units are given by $n = c_s = 1$, where n is the number density of SPH particles and c_s is the local sound speed. With this choice,

velocities are in units of c_s, distances are in units of $n^{-1/3}$, and times are in units of $n^{-1/3}c_s^{-1}$. In practice, we implement $c_s = 1$ by choosing the entropy variable $A = \rho^{1-\gamma}/\gamma$. Furthermore, the mass of the particles is chosen such that the cubical box contains unit mass: $M = Nm = 1$. Since the local number density and sound speed are known in any SPH calculation, these units make our results applicable to many contexts.

After positioning the particles on a regular lattice and assigning their velocities (with zero net momentum), we allow the system to evolve, without AV. Although each SPH particle represents a fluid element with a certain temperature and density, the SPH particles themselves have their own numerical "temperature" (due to the particle velocity dispersion) and number density. While there is an obvious correlation between the number density of the SPH particles and the density of the gas being represented, no such correlation exists between the numerical temperature of the SPH particles and the physical temperature of the gas being simulated. Regardless of the initial velocity distribution chosen, the velocities ultimately settle into an equilibrium Maxwell–Boltzmann distribution (see Fig. 1), and we then begin to study particle diffusion. We use the root mean square particle velocity $v_{\rm rms}$ to quantify the system's noise level, or numerical temperature. We have also found that the velocity distribution in real calculations tends to be roughly a Maxwellian centered on the local smoothed velocity. The energy exchange which causes thermalization is due to the strong coupling between neighboring particles through Eq. (10).

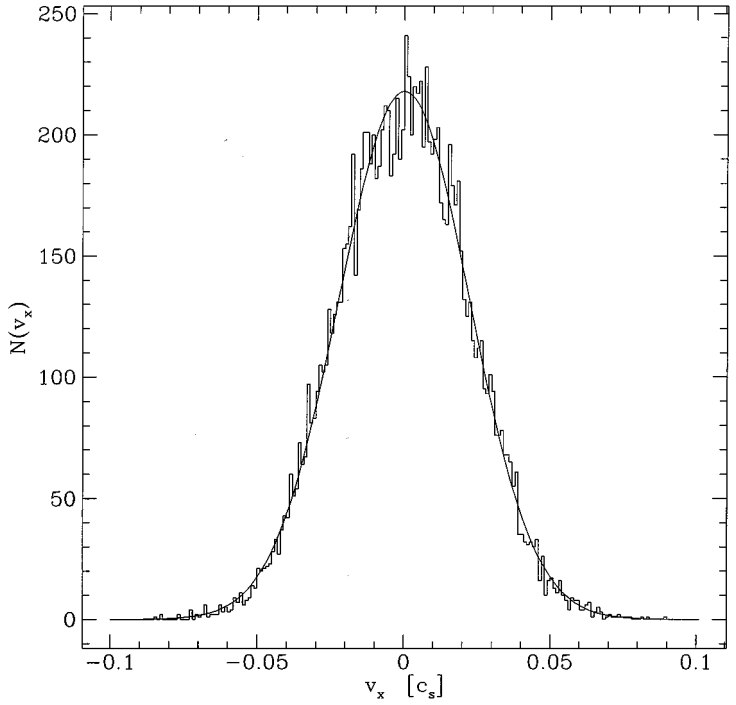

FIG. 1. The number of particles $N(v_x)$ in velocity bins of width $0.001c_s$ for the equilibrium state in a typical simple box test, where c_s is the sound speed. The $N = 23^3$ particles interacted with $N_N \approx 64$ neighbors and began in a simple cubic lattice configuration with noise artificially introduced at $t = 0$. The solid line shows the best fit Maxwellian, corresponding to $v_{\rm rms} = 0.404$, once the system has reached equilibrium. Deviations from this best fit are consistent with statistical fluctuations.

The level of diffusion is quantified as follows. Once the velocity distribution has settled into an equilibrium Maxwellian, we record the positions of all particles. Since ideally the particles would not move far from their initial positions, it is then easy to monitor the mean square spurious diffusion distance δ^2 as a function of time t (properly accounting for particles which cross the faces of the box). At late times the mean square deviation δ^2 increases at an nearly constant rate, so that the system obeys the usual diffusion equation $\delta^2 = Dt$, and the diffusion coefficient $D \equiv d\delta^2/dt$, evaluated at late times, is easily measured. (In molecular dynamics, the diffusion coefficient D is sometimes defined to be a factor of six smaller than in our definition.) As an example, Fig. 2 shows δ^2 and $d\delta^2/dt$ for a system with an equilibrium $v_{\rm rms} = 0.069$; it is clear that $d\delta^2/dt$ is essentially constant at late times, and we measure $D \approx 0.024$.

Figure 3 shows the diffusion coefficients D for various $v_{\rm rms}$ and for $N_N = 20$, 32, 48, and 64. Not surprisingly, spurious diffusion increases as $v_{\rm rms}$ increases. Note that, for a given N_N, there is a critical noise level below which the diffusion coefficient D is essentially zero. In this regime, the SPH particles settle into a regular lattice and oscillate around their equilibrium positions, and we say the system has "crystallized" (see Subsection 3.2). There seems to be a crystallization point for all the curves at some critical velocity dispersion $v_{\rm cr} > 0$. The trend is for $v_{\rm cr}$ to decrease as N_N increases. During the dynamical phase of real applications, AV typically keeps the noise level low enough that the numerical temperature is at most slightly above that required for crystallization.

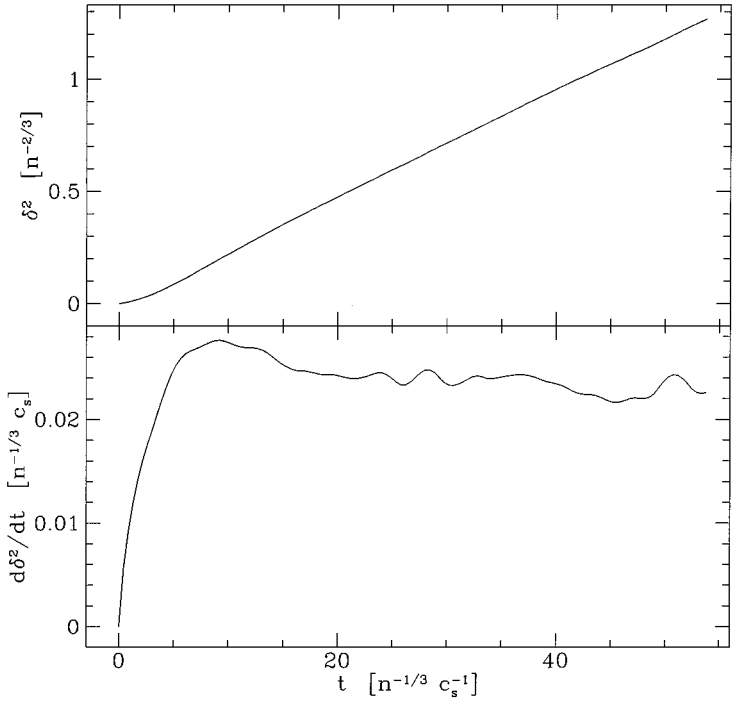

FIG. 2. The mean square deviation δ^2 and slope $d\delta^2/dt$ as a function of time after an equilibrium particle velocity dispersion $v_{\rm rms} = 0.069 c_s$ has been reached in a typical simple box test with $N_N = 48$ and no AV. At late times, the mean square deviation δ^2 increases approximately linearly with time, and we define the diffusion coefficient D as the slope of this line. Units are discussed in Subsection 3.1.

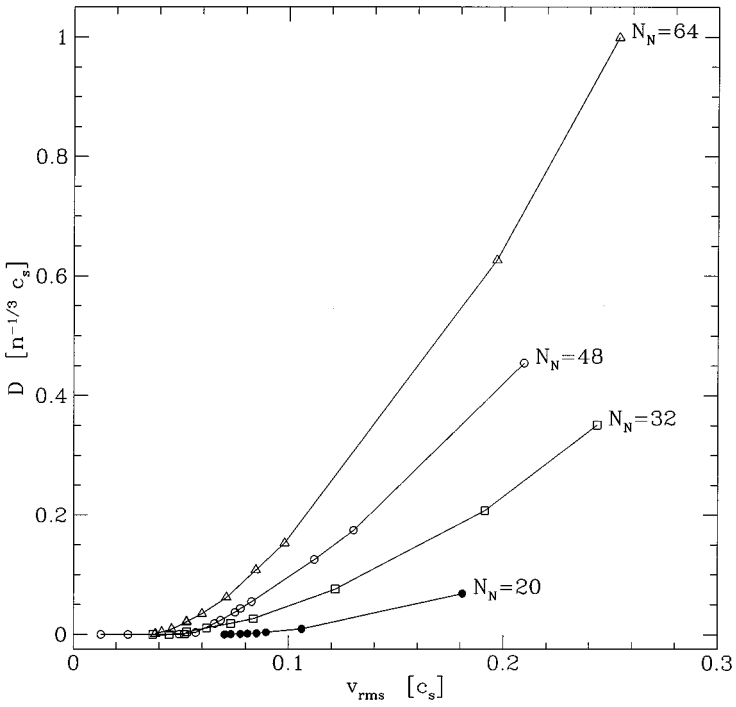

FIG. 3. The diffusion coefficient D as a function of the root mean square velocity dispersion $v_{\rm rms}$ for various neighbor numbers N_N, as measured by simple box tests in which the SPH particles began on a simple cubic lattice.

The diffusion coefficient is not always a unique function of N_N and $v_{\rm rms}$, but can also depend on the history of the SPH particles. To demonstrate this we started the particles on various types of lattices. Figure 4 shows the measured values of the diffusion coefficient D in the crystallization regime for systems of particles which began in either face centered cubic (dashed lines) or a simple cubic (solid lines) configurations. There is a clear dependence on the system's history in this regime, making it impossible to define a precise crystallization velocity dispersion. Note that all of the data points in Fig. 4 have a small diffusion coefficient, $D < 0.025$. Well above the crystallization noise level (that is, outside of the region displayed in Fig. 4) the diffusion coefficient is largely independent of initial conditions, that is, there is negligible history dependence for sufficiently large $v_{\rm rms}$.

The diffusion coefficients shown in Figs. 3 and 4 are measured while integrating the entropy equation (21) with a Courant number $C_N = 0.4$ and with the S timestep algorithm (see Eqs. (22), (23), and (24)). However, measurements which use the energy equation (20) or different Courant numbers, or both, give similar coefficients, provided only that the Courant number is small enough that the integration routine is stable.

3.2. *Lattices of SPH Particles*

By experimenting with various lattice types as initial conditions in the simple box tests, we have found that not all equilibrium configurations of SPH particles are stable. For example, for neighbor numbers in the range we explored ($32 \leq N_N \leq 64$), simple cubic lattice

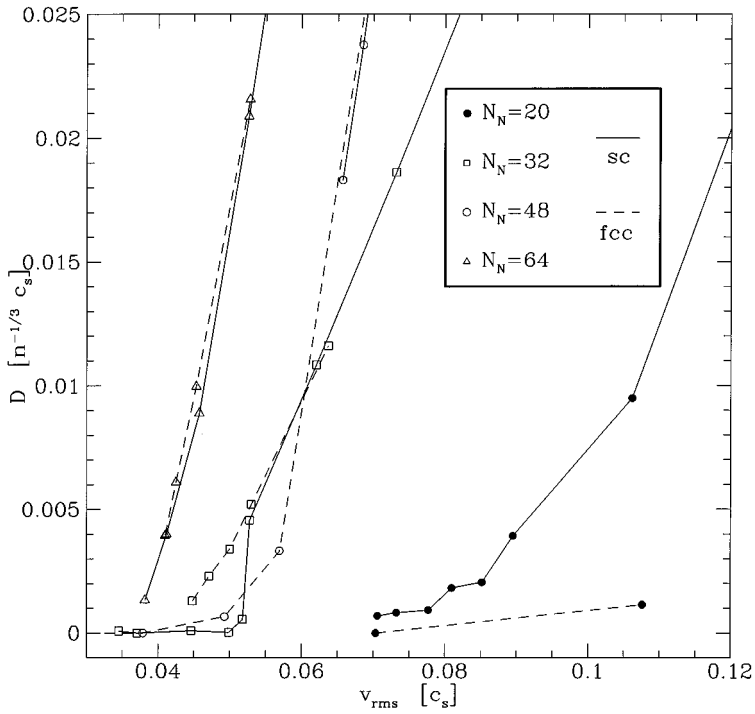

FIG. 4. The diffusion coefficient D near crystallization. Conventions are as in Fig. 3. At $t = 0$, the SPH particles began on either a simple cubic lattice (data points connected by solid lines) or a face centered cubic lattice (data points connected by dashed lines). In this regime, D has an obvious dependence on this system's history.

configurations are unstable to perturbations, while other lattice types, such as hexagonal close-packed, are stable. If the particles begin motionless and slightly perturbed from equilibrium simple cubic lattice sites, they achieve a non-zero noise level and readjust their positions to a different, preferred lattice type (see Fig. 5). The instability develops more slowly for smaller C_N, but it cannot be avoided altogether. Although the introduction of AV suppresses these instabilities, AV is almost always turned off during the relaxation calculations necessary to produce initial conditions for real dynamical simulations. Therefore, starting relaxation simulations in a stable lattice structure would avoid unnecessary phase transitions.

For a few of our simple box tests, we allowed the smoothing lengths h_i to vary both in time and in space, *without* including the corrections in the evolution equations described by Nelson and Papaloizou [51, 52] and Serna *et al.* [53]. The system's behavior is greatly affected: there is a secular, spurious increase in the total energy E. Almost all of this spurious energy is kinetic. If the AV is active during such runs, energy conservation is much better; however, the error then emerges as a spurious entropy increase (see Fig. 6). The AV run in Fig. 6 used $\alpha = 1$, $\beta = 2$, $\eta^2 = 0.01$, and the classical form of AV; both runs use $C_N = 0.8$ and an initial Maxwell–Boltzmann velocity distribution with a velocity dispersion $v_{\rm rms} = 0.107$.

In many SPH applications, shocks play an important role in the dynamics. Therefore, understanding how various AV schemes affect the level of spurious diffusion is essential. A uniform SPH gas is *not* an appropriate arena to study this effect, since the AV quickly solidifies the particles into a lattice structure. In a calculation with AV but without shocks

or shear, the diffusion coefficient D is always essentially zero (see Figs. 7 and 8), since diffusion occurs only as a transient.

We can derive approximate analytic expressions for the artificial viscous dissipation timescale by dimensional analysis on the AV term in Eq. (10). Here we focus on the classical AV (Eq. (11)); in Subsection 6.2 we will analyze all three AV forms in a different context. Beginning with Eq. (12), we note that since $|\mathbf{r_i} - \mathbf{r_j}| \sim h_{ij}$ we have $\mu_{ij} \sim \Delta v$, where Δv is a typical relative velocity of neighboring particles. If, in the vicinity of particles i and j, the sound speed is c_s and the density is ρ, then Eq. (11) gives us $\Pi_{ij} \sim -\alpha \Delta v c_s/\rho$ if $\beta \Delta v \ll \alpha c_s$ (as is typically the case in the absence of shocks). If the local number density of particles is n, then a typical particle mass $m_j \sim \rho/n$, and $|\boldsymbol{\nabla}_i W_{ij}| \sim n/(hN_N)$. Combining these expressions, we find that the acceleration of particle i due to the AV is

$$\dot{v}_i^{AV} \equiv \left| -\sum_j m_j \Pi_{ij} \boldsymbol{\nabla}_i W_{ij} \right| \sim \frac{\alpha c_s \Delta v}{h N_N^{1/2}}, \tag{26}$$

where we have assumed that the sum over N_N terms in Eq. (10) scales as $N_N^{1/2}$ since there is no preferred direction for $\boldsymbol{\nabla}_i W_{ij}$.

The artificial viscous dissipation timescale τ is then just $v/\dot{v}^{\mathrm{AV}}$, where v is a typical particle velocity. For the simple box tests we have $v \sim \Delta v \sim v_{\mathrm{rms}}$, so that the viscous timescale is

$$\tau \sim \frac{h N_N^{1/2}}{\alpha c_s} = \left(\frac{3}{32\pi}\right)^{1/3} \frac{N_N^{5/6}}{\alpha} n^{-1/3} c_s^{-1}. \tag{27}$$

Our numerical results agree well with this simple expression. For $\alpha = 1$ and $N_N = 32$, Eq. (27) gives a timescale $\tau \sim 6 n^{-1/3} c_s^{-1}$, which is approximately the time it takes to form a lattice (*i.e.*, the timescale on which the kinetic energy drops to zero) in the case presented in Fig. 7. Although the timescale depends on both N_N and the AV, it is always quite short: typically just a few sound crossing times between neighboring SPH particles.

4. POLYTROPE TESTS

Applications of SPH often involve self-gravitating systems with significant density gradients. The results of our simple box tests can be applied to such calculations, which we will demonstrate by considering a set of equilibrium $n = 1.5$ polytropes (spherical hydrostatic equilibrium configurations with $p = \mathrm{const} \times \rho^{1+1/n}$) all with mass M and radius R, but modeled with various total numbers N of equal mass particles and neighbor numbers N_N. In this section, all calculations implement the simple timestep routine given by Eqs. (22)–(24) and have no AV. The natural units are given by $G = M = R = 1$, so that consequently the unit of time is $(R^3/GM)^{1/2}$.

We relax the polytrope to equilibrium by applying an artificial drag force which opposes motion for 20 time units. We then remove the drag force and record the particle positions. Ideally, the particles would remain stationary. However, as expected from the results of Subsection 3.1, these particles spuriously diffuse from their starting positions, and this diffusion is easy to monitor. By periodically noting the particle velocity dispersion v_{rms}, we can apply the simple box test results to get an "instantaneous" value for the diffusion coefficient D by interpolating between data points in Fig. 3. In this way, we estimate the

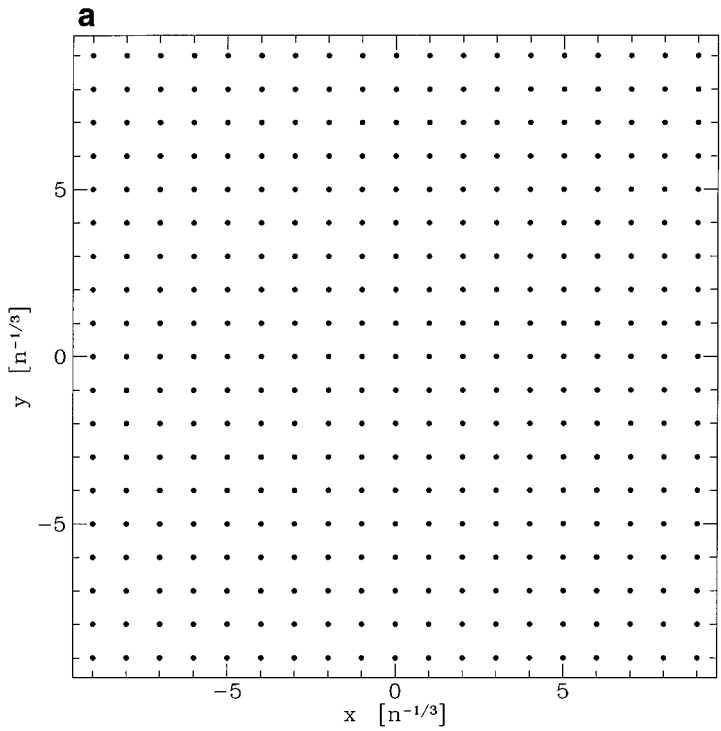

FIG. 5. This sequence of cross-sectional slabs, each of thickness $\Delta z = 1.02n^{-1/3}$, in a periodic box of dimension $19n^{-1/3} \times 19n^{-1/3} \times 19n^{-1/3}$ demonstrates the instability of a simple cubic lattice. (a) At $t = 0$ the $N = 19^3$ equal mass SPH particles, each with $N_N \approx 32$ neighbors, are initially motionless with only minuscule deviations (due to numerical roundoff errors) from the unstable equilibrium positions of a simple cubic lattice. (b) At $t = 190n^{-1/3}c_s^{-1}$ the particles are in the process of shifting their positions. (c) By $t = 380n^{-1/3}c_s^{-1}$ the particles have settled into a new, stable lattice structure.

mean square displacement δ^2 by a simple, numerically evaluated integral,

$$\delta^2 = \int D(t)\, dt, \tag{28}$$

and then compare this estimation to the actual, measured mean square displacement.

Figure 9 shows, as a function of time, the mean square spurious displacement for the innermost 6400 particles in an $n = 1.5$ polytrope modeled with $N = 13{,}949$ particles, each with $N_N = 48$ neighbors on average. We do not track the particles of the outer layers here, since they are subject to an effect which we do not attempt to model: when such a particle diffuses outward beyond the surface, gravity pulls it back, making the actual diffusion distance somewhat smaller than estimated. For those particles which always remain inside the surface, gravity is everywhere balanced by pressure gradient forces, so that the rate of diffusion is essentially the same as in our simple box tests. The usual advection scheme Eq. (7) was used for the calculation presented in the top frame of Fig. 9, while the XSPH Eq. (8) with $\epsilon = 0.5$ was used in the bottom frame. The estimated mean square displacement (dashed curve), as calculated from Eq. (28), agrees well with the actual square displacement (solid curve). To estimate the displacement in the XSPH calculation, the root mean square of the right hand side of Eq. (8) was used in place of $v_{\rm rms}$ when determining the diffusion coefficient D. The Courant number $C_N = 0.8$ and the simple timestep routine determine the integration timesteps for both cases.

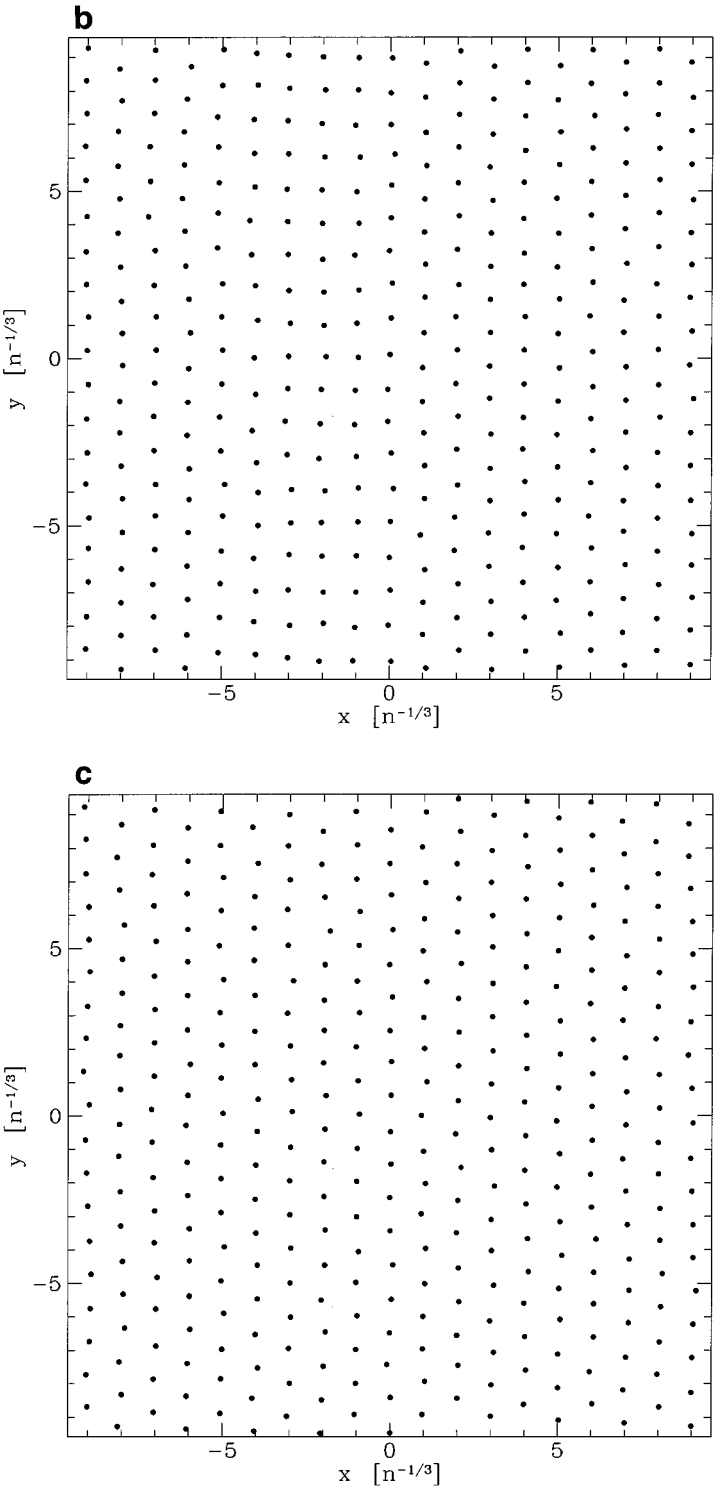

FIG. 5—*Continued*

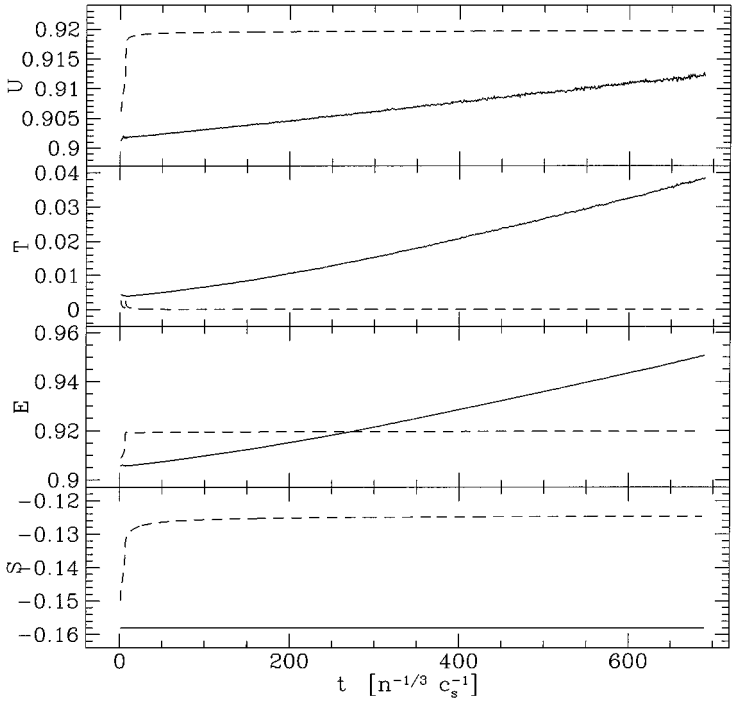

FIG. 6. The internal energy U, kinetic energy T, total energy $E = U + T$, and entropy S of the $N = 20^3$ equal mass particles interacting with $N_N \approx 64$ neighbors for a calculation without AV (solid curve) and a calculation with AV (dashed curve). In contrast to the previous simple box tests, the smoothing lengths h_i are allowed to vary. The particles began on a simple cubic lattice with a Maxwell–Boltzmann velocity distribution.

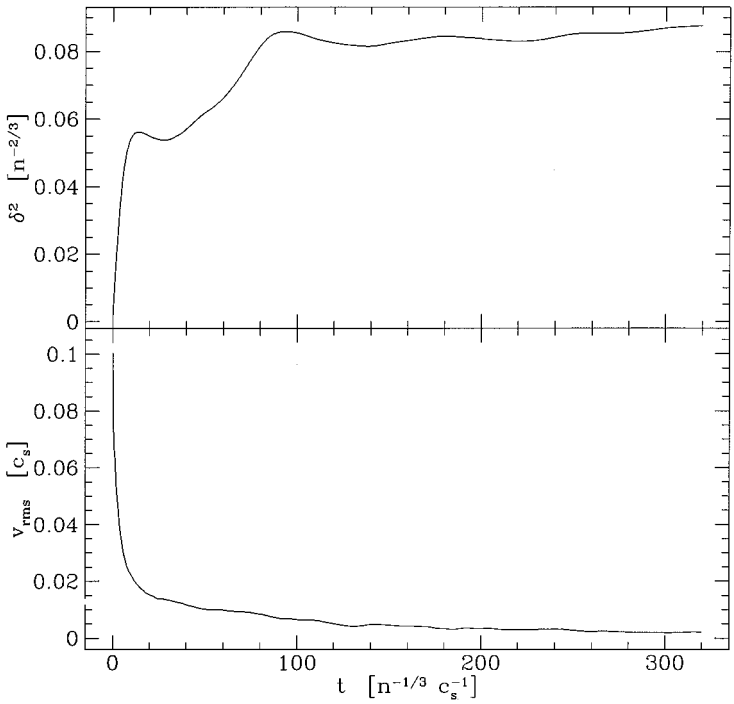

FIG. 7. The mean square deviation δ^2 and root mean square velocity $v_{\rm rms}$ as a function of time for $N = 16^3$ equal mass SPH particles with $N_N \approx 32$ in a typical simple box test. Here the AV is given by Eq. (11) with $\alpha = 1$, $\beta = 2$ and $\eta^2 = 0.01$. The particles begin in a simple cubic lattice with a Maxwell–Boltzmann velocity distribution. The AV drives $v_{\rm rms}$ to zero, so that the mean square deviation δ^2 approaches a constant and the diffusion coefficient $D = d\delta^2/dt$ becomes zero.

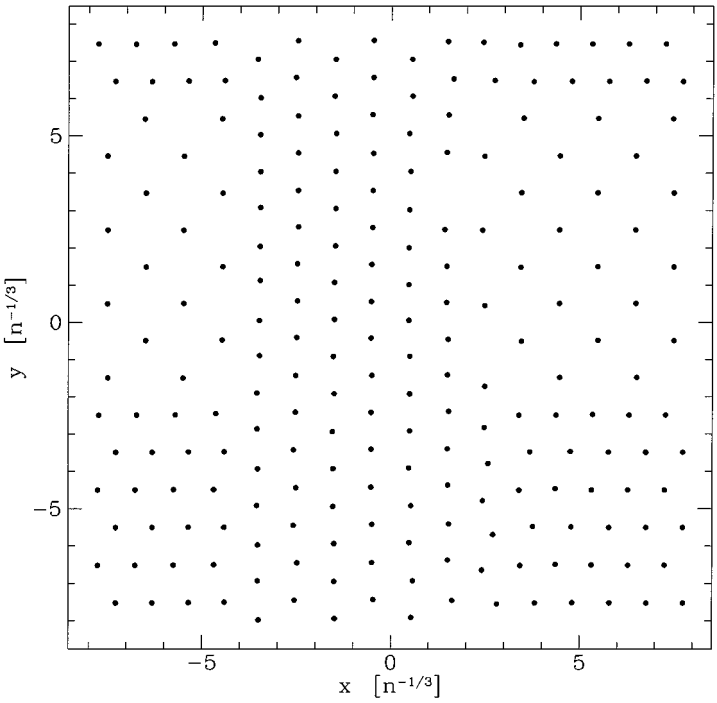

FIG. 8. A cross-sectional slab of thickness $\Delta z = 0.6n^{-1/3}$ of the final particle configuration for the simple box test presented in Fig. 7. There are clear dislocations separating the different lattice orientations. The initially noisy system has been quenched, or "frozen," into a crystal by the AV so quickly that the SPH particles did not have opportunity to settle into a single orientation.

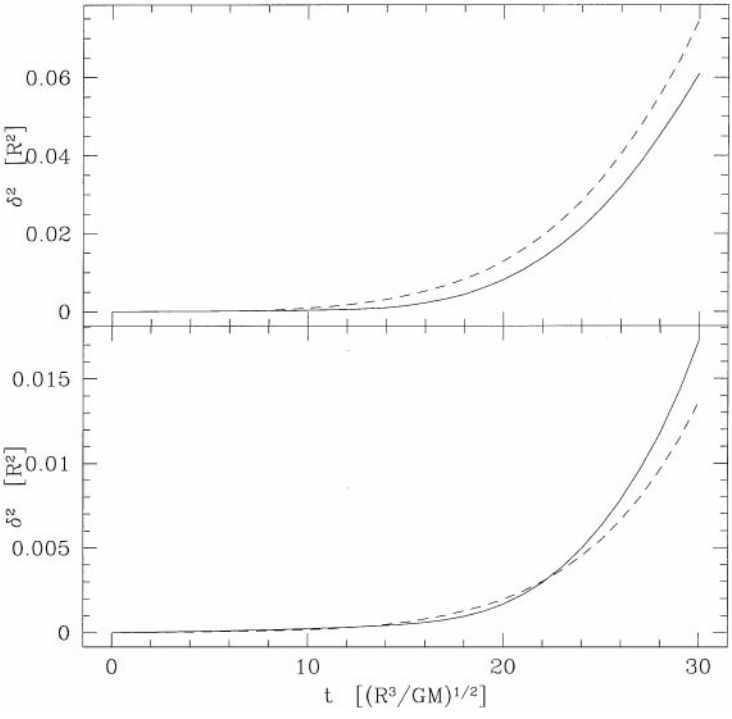

FIG. 9. The estimated (dashed curve) and actual mean square displacement (solid curve) for the innermost 6400 particles in an equilibrium $n = 1.5$ polytrope of mass M and radius R modeled with $N = 13949$ equal mass particles and $N_N \approx 64$. For the top frame Eq. (7) is used to update particle positions, while in the bottom frame Eq. (8), the XSPH method, is implemented.

The slight differences between estimated and actual displacements arise because of our interpolating to obtain D and because our diffusion coefficients are only approximate in the crystallization regime (due to history dependence). Since the SPH particles are melting out of their crystalline phase around $t \approx 10$, our values for D are overestimated then. The XSPH advection method does indeed diminish the amount of spurious diffusion: the final ($t = 30$) mean square displacement for the XSPH calculation is nearly one fourth of the value from the simple advection scheme. However, one must be careful when using XSPH: using too large of an ϵ can cause certain modes to become numerically unstable. For instance, for the extreme case of $\epsilon = 1$ we are not able to evolve an equilibrium $n = 1.5$ polytrope without the integration becoming unstable.

Figure 10 shows $\Delta E/E$, $(v/c_s)_{\rm rms}$, and δ^2/R^2 at $t = 25$ for a set of calculations with $C_N = 0.8$ and various N_N. Here the $n = 1.5$ polytropes are modeled by either $N = 30{,}000$ particles (circular data points) or $N = 13{,}949$ particles (square data points). For a given N_N, the $N = 30{,}000$ models always have larger accumulated errors: as N is increased, one must also increase N_N in order for the SPH scheme to remain accurate. Although increasingly larger N_N results in increasingly smaller errors, this does not mean one should strive to use as large a value for N_N as possible. Large N_N yields large smoothing lengths and hence poor spatial resolution. The optimal N_N must be determined by a compromise between the competing factors of accuracy and resolution and depends on the particular application. Nevertheless, we can place very loose constraints on how fast the optimal N_N should be increased as N is increased. From Fig. 10 we see that in going from $N = 13{,}949$ to $N = 30{,}000$ we need to increase N_N by at least (very roughly) 15% in order to prevent the

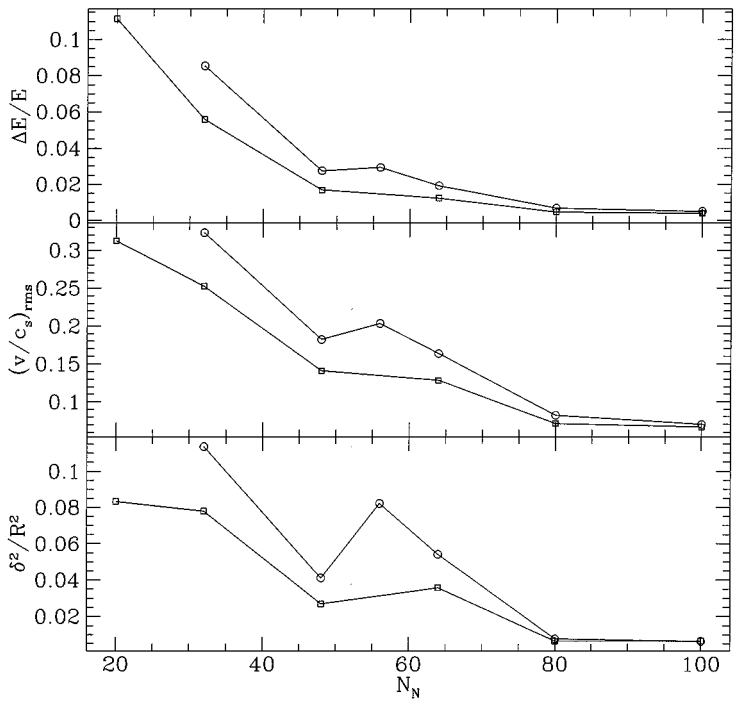

FIG. 10. The fractional spurious change in total energy $\Delta E/E$, $(v/c_s)_{\rm rms}$ and the mean square diffusion distance δ^2 as a function of N_N evaluated at a time $t = 25(R^3/GM)^{1/2}$ during calculations of an equilibrium $n = 1.5$ polytrope. Circular data points correspond to a polytrope modeled with $N = 30{,}000$ particles, while square data points correspond to those with $N = 13{,}949$ particles.

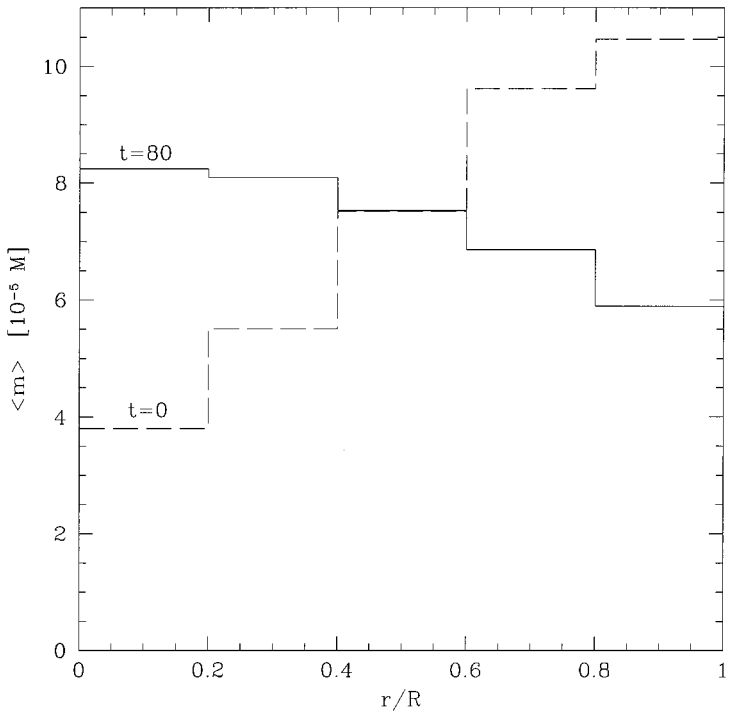

FIG. 11. Histogram of the average SPH particle mass $\langle m \rangle$ in five radial bins for the initial configuration (dashed curve) and $t = 80(R^3/GM)^{1/2}$ configuration (solid curve) during the evolution of an equilibrium $n = 1.5$ polytrope of mass M and radius R. This calculation employs $N = 13{,}949$ particles with $N_N \approx 64$, $C_N = 0.8$, the simple timestep routine, and no AV.

errors from increasing. This corresponds to a scaling $N_N \propto N^q$ with $0.2 \lesssim q < 1$, assuming a power-law relation. The upper limit of 1 on q stems from the requirement that the smoothing lengths must decrease as N and N_N increase.

SPH calculations sometimes use particles of unequal mass so that less dense regions can still be highly resolved. Unfortunately, the more massive particles tend to diffuse to the bottom of the gravitational potential more so than less massive ones. In other words, each particle has a preferred direction to diffuse, and in a dynamical application this direction can be continually changing. As an example, we evolved an equilibrium $n = 1.5$ polytrope in which the SPH particles initially in the envelope were, on average, heavier than those in the core. Over the course of the calculation, the heavier particles settled to the core while the lighter particles tended to the envelope (see Fig. 11). Such behavior makes spurious diffusion more difficult to estimate in calculations which use unequal mass particles.

5. PERIODIC SHOCK-TUBE TESTS

Since the simple box tests of Section 3 are helpful only for calculations without AV, we turn now to a periodic version of the 1D Riemann shock-tube problem of Sod [56], a standard test of hydrodynamic codes and AV schemes containing many of the same qualitative features as real applications which involve shocks. The physical setup is as follows.

Initially, fluid slabs with constant (and alternating) density ρ and pressure p are separated by an infinite number of planar, parallel, equally spaced interfaces. We define the unit of length to be twice the distance between adjacent interfaces, and let the $x = 0$ plane coincide

with one of these interfaces, so that

$$\begin{aligned} \rho &= \rho_l, \qquad p = p_l \quad \text{if } -\tfrac{1}{2} < x \le 0 \\ \rho &= \rho_r, \qquad p = p_r \quad \text{if } 0 < x \le \tfrac{1}{2}, \end{aligned} \tag{29}$$

where ρ_l, p_l, ρ_r, and p_r are constants specifying the density and pressure of the slabs to the "left" and "right" of $x = 0$. Pressures and densities for $|x| > \frac{1}{2}$ are given by repeatedly stacking the thermodynamic slabs described by Eq. (29) along the x-axis to infinity, hence the name *periodic* shock-tube tests. At $t = 0$ the interfaces are removed and, if $p_l \neq p_r$, a shock wave moves from the high pressure material into the low. A rarefaction wave also originates at each interface, propagating in the direction opposite to its corresponding shock. Before the initial collision of shock waves from adjacent interfaces, regions of five different thermodynamic states coexist and the entropy of the fluid increases linearly with time. A quasi-analytic solution can be constructed for these early times using standard methods (see, e.g., [57]) and is presented in detail by Rasio and Shapiro [54].

5.1. *Low Mach Number Cases*

For the first set of shock-tube calculations we consider, the fluid slab to the left of the interface at $x = 0$ initially has density $\rho_l = 1.0$ and pressure $p_l = 1.0$, while on the right $\rho_r = 0.25$ and $p_r = 5/2^{16/3} = 0.12402$. Consequently this box contains 0.625 units of mass: 0.5 on the left and 0.125 on the right. An adiabatic equation of state is used with $\gamma = 5/3$, so that the entropy variable A equals 1.0 on the left and 1.25 on the right. From Eq. (6), the initial entropy of each of the periodic cells is thus $S = 1.5[0.5\ln(1.5) + 0.125\ln(1.5 \times 1.25)] = 0.4220$. For these initial conditions, the initial shock waves have a relatively low Mach number $\mathcal{M} \approx 1.6$. In these units, the speed of sound in the initial left hand slab is $c_s^l = (\gamma p_l/\rho_l)^{1/2} = \gamma^{1/2}$, and the unit of time is therefore $\gamma^{1/2} L/c_s^l$, where L is the length of a periodic cell (our unit of length).

Employing the classical AV of Eq. (11), we obtained a good representation of the shock with our 1D code by using $\alpha = \beta = 1$ and $\eta^2 = 0.05$. The smoothing length h of the $N = 2500$ equal mass particles was constant and chosen such that the particles would have $N_N = 16$ neighbors on average. Our 1D code integrates the energy equation and uses the Monaghan timestep routine with $C_N = 0.2$. Figure 12 shows the density and velocity profiles as given by the quasi-analytic solution (solid curve) and our 1-dimensional code (dotted curve) at a time $t = 0.15$. As expected, discontinuities are smoothed over a few smoothing lengths. Figure 13 shows the entropy (see Eq. (6)) given by our 1D SPH code (dotted curve), which nearly matches the quasi-analytic solution (solid curve).

The above calculation helps establish the accuracy of our 1D code, but does not assess the accuracy of a 3D calculation, where the much smaller number of particles per dimension leads to a reduced spatial resolution. Furthermore, numerical errors, including spurious mixing, are artificially reduced for motion with only one degree of freedom. We test our 3D code with the same physical problem: at $t = 0$, slabs of fluid with alternating thermodynamic states are separated by equally spaced planar interfaces perpendicular to the x-axis. Periodic boundary conditions are imposed on all six sides of a cube with faces at $x = \pm\frac{1}{2}$, $y = \pm\frac{1}{2}$, and $z = \pm\frac{1}{2}$. We consider cases only with a constant smoothing length $h \ll 1$, and, unless otherwise stated, we integrate the entropy equation.

Our calculations with the 3D code use $N = 10^4$ equal mass particles. All the particles initially in the left hand slab have the same smoothing length, smaller than the smoothing

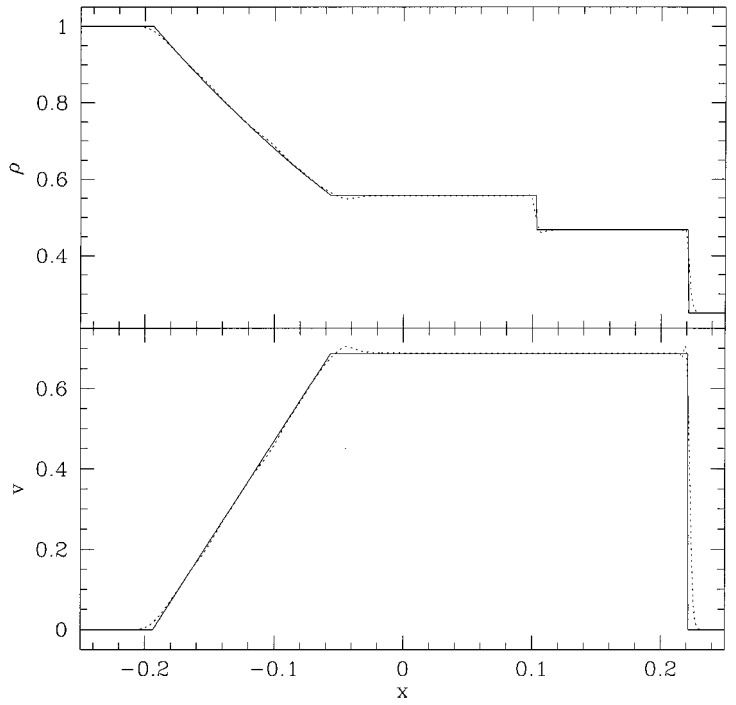

FIG. 12. Density and velocity profiles in a shock-tube test with Mach number $\mathcal{M} \approx 1.6$ as given by the quasi-analytic solution (solid curve) and our 1-dimensional SPH code (dotted curve) at a time $t = 0.15$. An adiabatic equation of state is used with $\gamma = 5/3$.

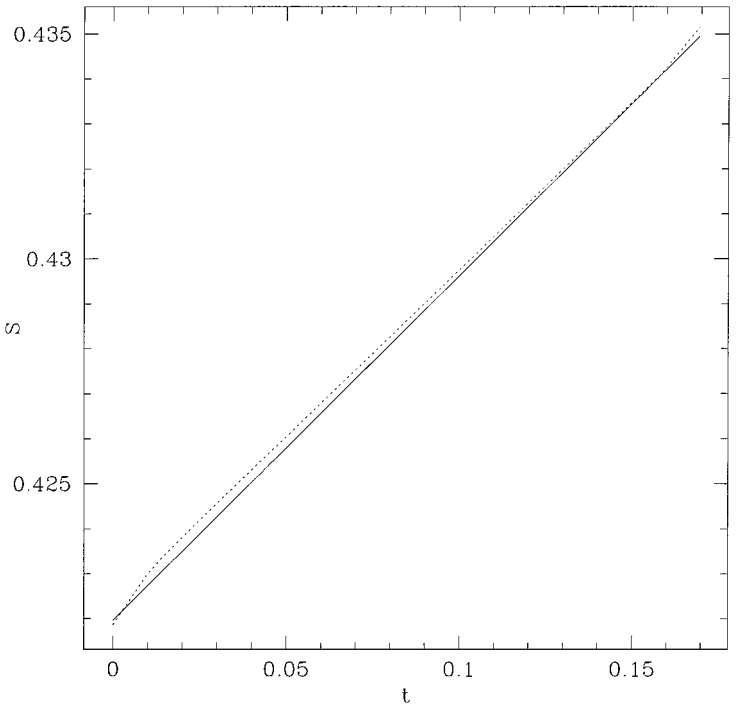

FIG. 13. Entropy S in a shock-tube at early times t, as given by the quasi-analytic solution (solid line) and our 1D SPH code (dotted curve), for the same calculation presented in Fig. 12.

length common to particles initially in the right hand slab. These smoothing lengths are not allowed to vary with time and are chosen such that particles which are farther than $2h$ from an interface have $N_N = 64$ neighbors on average. Within each constant density slab, the SPH particles start in a stable lattice with a randomly chosen orientation (choosing the lattice face to be parallel to the interface would be too artificial of a setup). The initial conditions for each slab are constructed by randomly distributing particles in a periodic box of dimensions $\frac{1}{2} \times 1 \times 1$ and then slowly relaxing the system with an artificial drag force. The resulting lattices are preferred to initially randomly distributed particles, since a random distribution would introduce a high noise level not representative of real applications.

We determine the accuracy of our calculations with the 3D code by comparing its results against those of the much more accurate 1D code. Such 3D calculations are a useful and realistic way to calibrate spurious transport in simulations with AV, since the test problem, which includes shocks and some large fluid motions, has many of the same properties as real astrophysical problems. In fact, the recoil shocks in stellar collisions do tend to be nearly planar, so that even the 1D geometry of the shock fronts is realistic. The periodic boundary conditions play the role of gravity in the sense that they prevent the gas from expanding to infinity.

Figure 14 shows the pressure P, entropy variable A, density ρ, and velocity v_x as given by our 1D code (solid curve) and by our 3D code (dots) at the relatively late time $t = 1$. Here the 3D calculation implements the classical AV with $\alpha = 0.5$ and $\beta = 1$. The bar in the lower left corner of the uppermost frame displays the average region of influence (i.e., the mean diameter of the smoothing kernels) for the particles in the 3D calculation: the total length of this bar is $4\langle h \rangle$, where $\langle h \rangle = 0.058$ is the average smoothing length. The 3D calculation does well at reproducing the major features in the thermodynamic profiles,

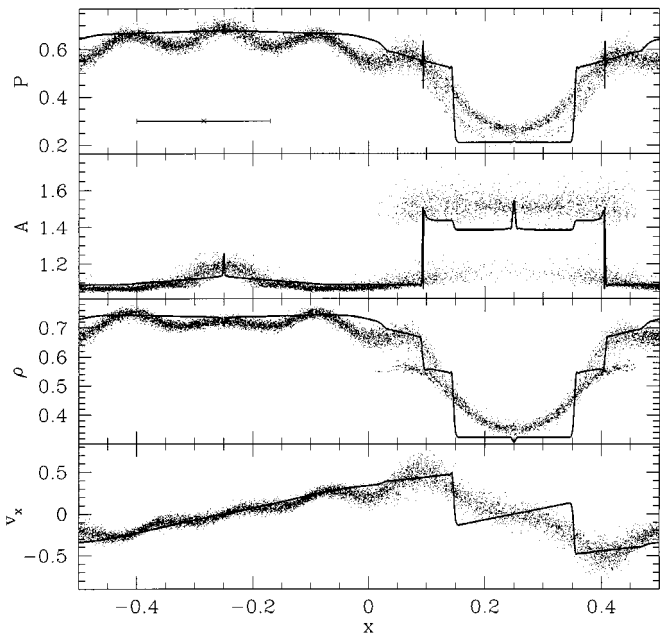

FIG. 14. The pressure P, entropy variable A, density ρ, and velocity component v_x as given by our 1D code (solid curve) and by one of our 3D calculations (dots) at the relatively late time $t = 1$, for the same shock-tube test shown in Figs. 12 and 13. The bar in the lower left corner of the uppermost frame has a total length of $4\langle h \rangle$, where $\langle h \rangle = 0.058$ is the average smoothing length in the 3D calculation.

but, not surprisingly, smoothes out any small scale structure which occurs on lengths scales shorter than a few smoothing lengths. In the regions near $x = 0.1$ and $x = 0.4$, where the fluid is being shock-heated, the pressure, entropy variable, and density in the 3D calculation are double-valued due to short-range particle interpenetration and to the shock front not remaining perfectly planar throughout the calculation.

Since the fluid in these calculations should move solely in the x-direction, spurious motion in the y- and z-directions is easy to measure. Spurious motion in the x-direction can be studied by the following method, based on the idea that planes of fluid should not cross in one dimension. That is, the shape of a composition profile should remain unchanged throughout a calculation. Once the shock-tube system has reached a steady state, we examine the distribution of the Lagrangian labels $x_i(t = 0)$ as a function of $m(x)$, the amount of mass between the interface (contact discontinuity) and x. Deviations from the initial profile must be spurious, so we can immediately calculate spurious displacements in the x-direction for individual particles. Diffusion measurements in each of the three directions give similar results.

We have studied the quality of the 3D code's results for various AV parameters and forms. We have completed a number of shock-tube tests which began with the same initial conditions described above, but with different values of the AV parameters. Varying η^2 by a factor of 25 between 0.002 and 0.050 makes little difference in the results, and we therefore concentrate on the effects of α and β. All calculations described in this section have $\eta^2 = 0.01$.

Figure 15 shows the dependence of the solution on α and β for the classical AV by plotting, as a function of time, the mean square spurious displacement in the directions perpendicular to the bulk fluid motion (in units of $n^{-1/3}$, where n is the SPH particle number density), the internal energy U, and the entropy S. The solid line results from our accurate calculation of the shock-tube problem with the 1D code. In frame (a) of Fig. 15, $\alpha = 0$ while β is varied. In (b), $\beta = 0$ and α is varied. Finally in (c), $\beta = 1$ and α is varied. Runs with $\alpha = 0$ or $\beta = 0$ are interesting since they represent an AV which is either purely quadratic (von Neumann–Richtmyer viscosity) or linear (bulk viscosity) in μ_{ij}, respectively, and these two types of AV generate different numerical viscosities (see Section 6).

Table I summarizes all of our low Mach number 3D shock-tube calculations and reports how well each does matching the 1D solution. All the calculations in Table I employed 10^4 particles and a fixed smoothing length chosen such that the number of neighbors $N_N = 64$ on average. In Column 1, we identify the type of AV used: C for the classical AV (Eq. (11)), HK for the Hernquist and Katz AV (Eq. (13)), and B for the Balsara AV (Eq. (16)). Columns 2 and 3 list the AV parameters α and β (unless otherwise noted $\eta^2 = 0.01$). Column 4 gives the type of timestep routine used: S for simple (Eq. (24)) and M for Monaghan (Eq. (25)). Column 5 gives the Courant number C_N. Columns 6 and 7 give the number of iterations required to reach $t = 1$ and $t = 4$, respectively. Column 8 gives the fractional deviation in the total energy away from its initial value: $\Delta E/E = |E(t = 4) - E(t = 0)|/E(t = 0)$. The $t = 4$ value of $\delta_y^2 + \delta_z^2$, the spurious displacement squared in the direction perpendicular to the bulk fluid flow, averaged over all particles, is listed in Column 9. Columns 10 and 11 give the maximum deviation in U/E and S, respectively, from that of the 1D code: $\Delta(U/E)_{\max} \equiv \mathrm{Max}|U_{3D}/E_{3D} - U_{1D}/E_{1D}|$ and $\Delta S_{\max} \equiv \mathrm{Max}|S_{3D} - S_{1D}|$.

Figure 16 shows, as a function of time, the average square displacement perpendicular to the bulk fluid flow $\delta_y^2 + \delta_z^2$, the ratio of internal to total energy U/E, and the entropy S for three calculations with different forms of AV: the classical AV with $\alpha = 0.5$, $\beta = 1$ (long

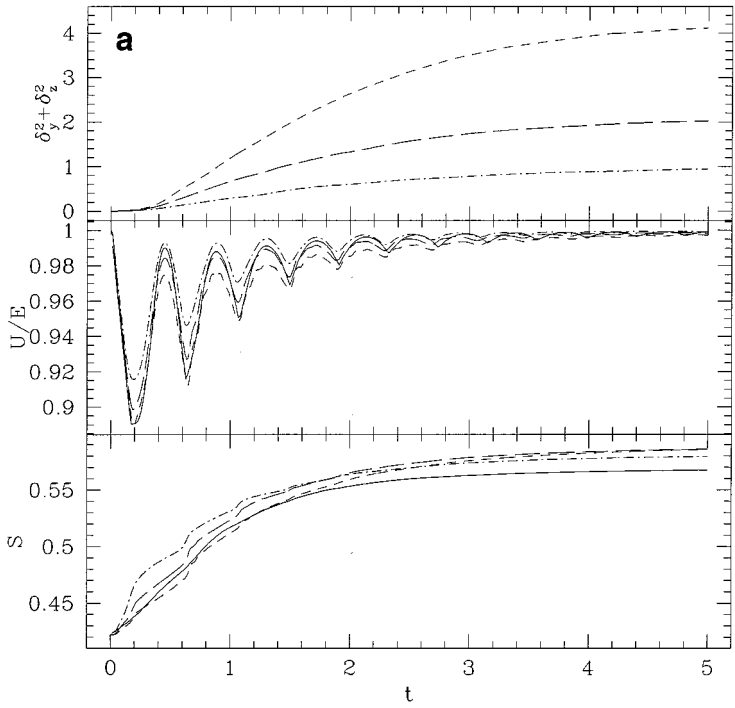

FIG. 15. Dependence of the results of shock-tube calculations on the AV parameters α and β for the classical AV with our 3D SPH code: (a) $\alpha = 0$; $\beta = 1$ (short), 2.5 (long), 10 (dot short), (b) $\beta = 0$; $\alpha = 1$ (short), 2 (long), 3 (dot short), 10 (dot long), (c) $\beta = 1$; $\alpha = 0$ (dot), 1 (short dash), 2 (long dash), 3 (dot dash). In all cases $\eta^2 = 0.01$. The solid line in the bottom two frames corresponds to our benchmark 1D calculation.

dashed curve), the HK AV with $\alpha = \beta = 0.5$ (short dashed curve), and the Balsara AV with $\alpha = \beta = \gamma/2$ (dotted curve). As we will discuss in Subsection 7.4, these choices for α and β are our recommended values. In the bottom two frames, the solid curve corresponds to our 1D SPH code. We see that all three AV forms can handle the shocks with roughly the same degree of accuracy, although the HK AV does allow slightly more spurious mixing and does not match the 1D code's U/E curve quite as well.

We also ran several low Mach number calculations with the energy equation being integrated. Table II compares these runs against the corresponding calculations in which the entropy equation was integrated. For given values of α, β, and η^2, the two schemes do equally well at conserving energy, at controlling particle diffusion, and at matching the time evolution of U/E from the 1D calculation. However, integrating the energy equation does allow slightly larger errors in the evolution of entropy, with $\Delta S_{\max}$ being 0.005 to 0.007 larger than when the entropy equation is integrated. This larger error in the entropy accumulates mostly at early times when the shocks are strongest.

5.2. *High Mach Number Cases*

Since many astrophysical situations involve shocks which are stronger than the low Mach number situation described in the previous section, we repeated shock-tube tests with a larger difference in pressure between the alternating fluid slabs. In particular, we initially set $p_l = 1.0$, $\rho_l = 1.0$, and $\rho_r = 0.25$ but reduced the pressure of the right-hand fluid slab to $p_r = 1.2402 \times 10^{-3}$, a factor of 100 less than in the low Mach number cases of

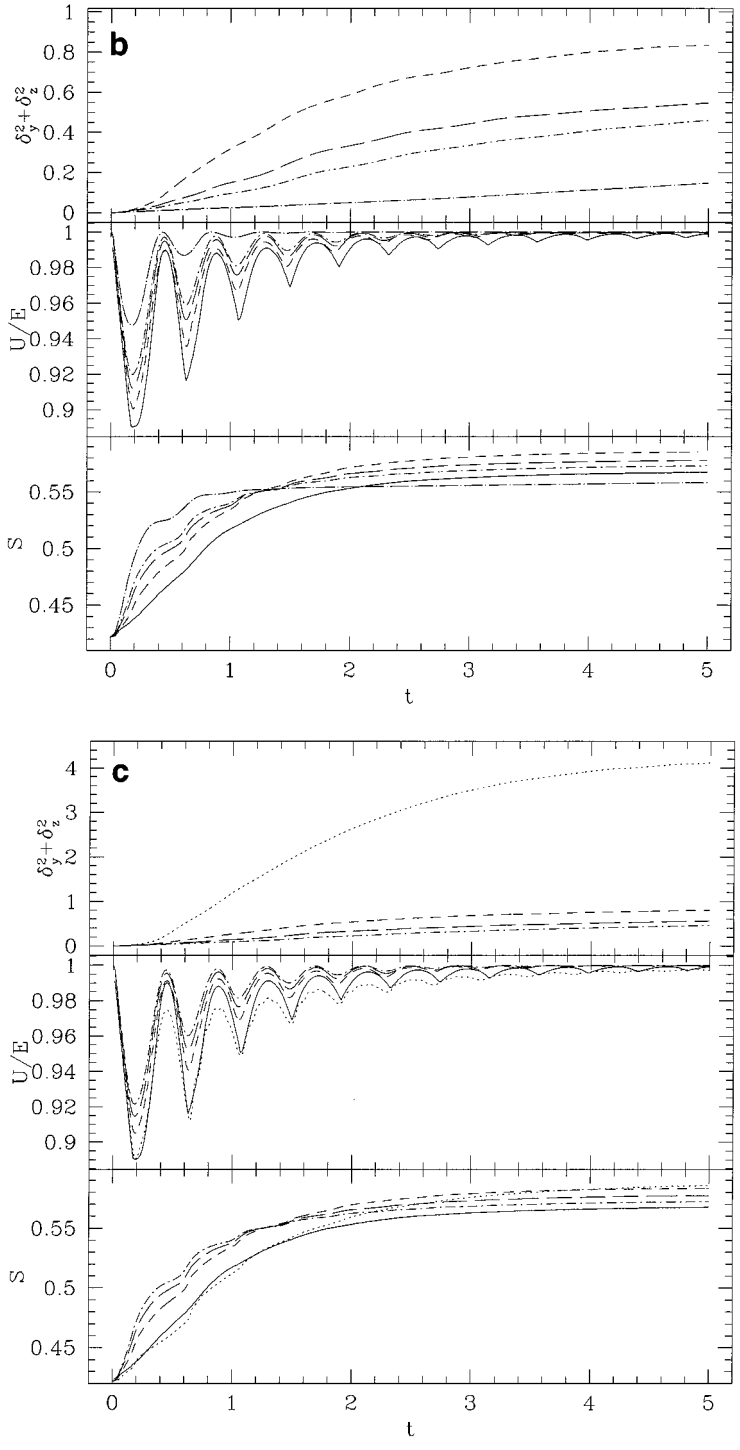

FIG. 15—*Continued*

TABLE I

Low Mach Number Shock-Tube Cases with $\gamma = 5/3$

AV routine	α	β	dt routine	C_N	Steps to $t=1$	Steps to $t=4$	$\Delta E/E$ at $t=4$	$\delta_y^2+\delta_z^2$ $[n^{-2/3}]$ at $t=4$	$\Delta(U/E)_{\max}$	$\Delta S_{\max}$
None			S	0.1	436	1664	0.06%	115.7	0.111	0.14
C	0	0.1	S	0.1	413	1402	0.04%	25.25	0.044	0.051
C	0	1	S	0.8	38	140	4.56%	3.16	0.014	0.025
C	0	2.5	S	0.1	295	1121	0.04%	1.92	0.014	0.018
C	0	10	S	0.1	281	1078	0.04%	0.88	0.030	0.030
C	0	100	S	0.1	307	1072	0.05%	0.40	0.064	0.064
C	0.1	1	M	0.3	163	572	0.13%	2.51	0.012	0.019
C	0.2	0.5	M	0.3	145	523	0.25%	2.43	0.013	0.019
C	0.2	1	M	0.3	167	585	0.11%	1.81	0.010	0.020
C	0.2	1	M	0.8	63	218	1.31%	1.81	0.013	0.011
C	0.2	1.25	M	0.3	175	612	0.07%	1.72	0.011	0.020
C	0.3	1	M	0.3	170	604	0.09%	1.54	0.012	0.020
C	0.5	1	M	0.3	180	653	0.08%	1.10	0.017	0.019
C	0.5	1	M	0.8	68	245	0.78%	1.09	0.016	0.015
C	1	0	S	0.8	36	134	1.41%	0.78	0.021	0.018
C	1	1	S	0.8	39	164	1.25%	0.76	0.025	0.020
C	1	1	M	0.8	81	307	0.41%	0.74	0.025	0.023
C	1	1.25	M	0.3	221	832	0.03%	0.76	0.026	0.025
C	1	2	S	0.8	42	171	0.92%	0.72	0.028	0.025
C	2	0	S	0.1	278	1063	0.02%	0.51	0.035	0.034
C	2	1	S	0.8	56	231	0.72%	0.52	0.040	0.049
C	3	0	S	0.1	275	1053	0.01%	0.41	0.043	0.042
C	3	1	S	0.8	79	329	2.18%	0.40	0.047	0.066
C	10	0	S	0.1	265	1035	0.24%	0.11	0.071	0.068
HK	0	1.25	M	0.3	116	449	0.28%	7.40	0.016	0.015
HK	0.1	0.5	M	0.3	111	440	0.40%	8.97	0.018	0.016
HK	0.1	0.5	M	0.8	42	161	2.79%	6.95	0.014	0.025
HK	0.1	1	M	0.8	45	171	2.00%	4.64	0.018	0.014
HK	0.1	2	M	0.8	52	191	0.98%	3.19	0.025	0.025
HK	0.2	0.5	M	0.3	117	463	0.31%	4.63	0.013	0.012
HK	0.2	0.75	M	0.3	119	467	0.24%	3.95	0.016	0.016
HK	0.3	0.5	M	0.3	125	493	0.22%	3.05	0.016	0.017
HK	0.4	0.5	M	0.3	135	534	0.15%	2.45	0.020	0.022
HK	0.5	0.5	M	0.3	145	572	0.11%	1.97	0.025	0.027
HK	0.5	1	M	0.3	148	579	0.06%	1.78	0.029	0.032
HK	0.5	1	M	0.8	56	218	0.43%	1.80	0.030	0.031
HK	1	0	M	0.3	196	768	0.01%	1.21	0.039	0.040
HK	1	1	M	0.3	198	772	0.02%	1.13	0.044	0.045
HK	1	1	M	0.8	75	291	0.32%	1.16	0.044	0.046
HK	1	1	S	0.8	39	151	4.70%	1.36	0.043	0.080
B	0	$2.5\times\gamma/2$	M	0.3	192	687	0.05%	5.11	0.012	0.011
B	$0.2\times\gamma/2$	$0.5\times\gamma/2$	M	0.3	144	534	0.28%	6.86	0.021	0.018
B	$0.5\times\gamma/2$	$1\times\gamma/2$	M	0.3	173	637	0.12%	1.98	0.010	0.019
B	$1\times\gamma/2$	$0.75\times\gamma/2$	M	0.3	206	800	0.09%	1.14	0.018	0.019
B	$1\times\gamma/2$	$1\times\gamma/2$	M	0.3	211	811	0.07%	1.13	0.019	0.020
B	$1\times\gamma/2$	$1\times\gamma/2$	M	0.8	79	304	0.54%	1.08	0.020	0.018
B	$1\times\gamma/2$	$1.25\times\gamma/2$	M	0.3	216	819	0.05%	1.12	0.020	0.020
B	$1\times\gamma/2$	$2\times\gamma/2$	M	0.3	305	1195	0.05%	0.74	0.031	0.031
B	$2\times\gamma/2$	0	M	0.3	233	855	0.02%	1.07	0.022	0.023
B	$2\times\gamma/2$	$1\times\gamma/2$	M	0.3	309	1212	0.04%	0.70	0.032	0.031
B	$2\times\gamma/2$	$1.25\times\gamma/2$	M	0.3	311	1213	0.03%	0.71	0.032	0.032

TABLE II
Low Mach Number Shock-Tube Cases with $\gamma = 5/3$ (Classical AV, Simple Timestep Routine, $C_N = 0.1$)

α	β	η^2	Evolution equation	Steps to $t=1$	Steps to $t=4$	$\Delta E/E$ at $t=4$	$\delta_y^2+\delta_z^2$ $[n^{-2/3}]$ at $t=4$	$\Delta(U/E)_{\max}$	$\Delta S_{\max}$
0	1	0.01	entropy	313	1172	0.04%	3.9	0.015	0.016
0	1	0.01	energy	335	1295	0.04%	4.1	0.016	0.021
1	0	0.01	entropy	285	1082	0.01%	0.8	0.021	0.023
1	0	0.01	energy	309	1222	0.01%	0.8	0.022	0.030
1	1	0.002	entropy	283	1076	0.01%	0.7	0.025	0.025
1	1	0.002	energy	306	1215	0.01%	0.8	0.024	0.032
1	1	0.01	entropy	283	1076	0.01%	0.8	0.025	0.025
1	1	0.01	energy	306	1210	0.01%	0.8	0.024	0.032
1	1	0.05	entropy	283	1079	0.01%	0.8	0.024	0.025
1	1	0.05	energy	307	1219	0.02%	0.8	0.024	0.031
2	1	0.01	entropy	278	1061	0.02%	0.5	0.036	0.035
2	1	0.01	energy	304	1197	0.00%	0.5	0.035	0.042
3	1	0.01	entropy	275	1053	0.01%	0.4	0.044	0.044
3	1	0.01	energy	304	1198	0.00%	0.4	0.044	0.050

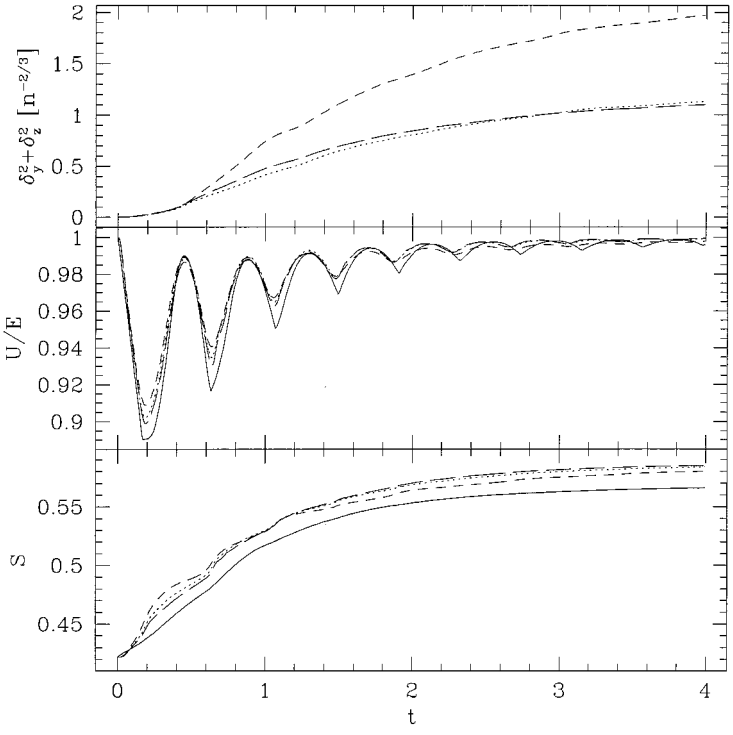

FIG. 16. The average square displacement perpendicular to the bulk fluid flow $\delta_y^2+\delta_z^2$, the ratio of internal to total energy U/E, and the entropy S for three $\gamma = 5/3$ shock-tube calculations with different forms of AV: the classical AV with $\alpha = 0.5$, $\beta = 1$ (long dashed curve), the HK AV with $\alpha = \beta = 0.5$ (short dashed curve), and the Balsara AV with $\alpha = \beta = \gamma/2$ (dotted curve). The solid curve in the bottom two frames results from our 1D SPH code.

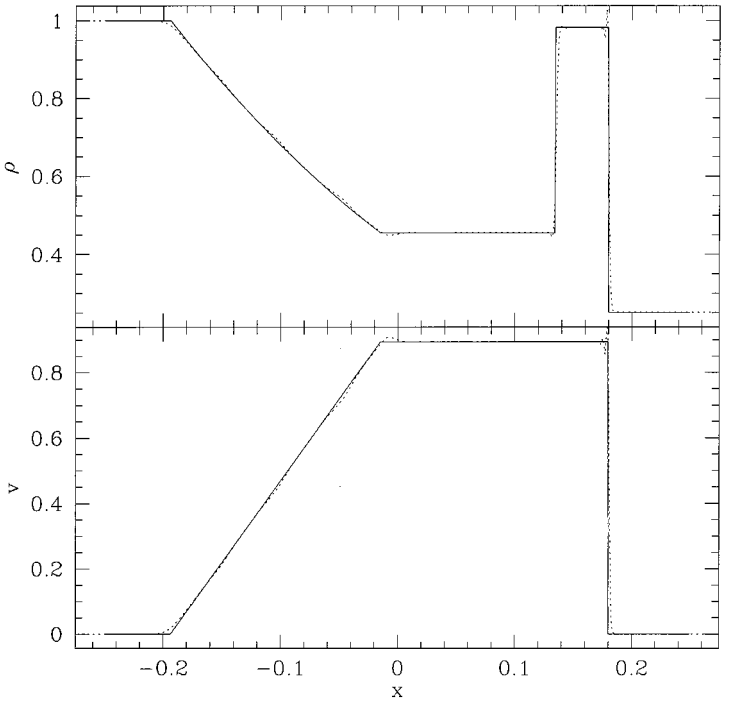

FIG. 17. The same situation as Fig. 12, but for a higher Mach number ($\mathcal{M} \approx 13.2$) shock-tube test. The solid line is the quasi-analytic solution, while the dotted line is the result of our 1D SPH code.

Subsection 5.1. This increases the Mach number of the initial shock waves to $\mathcal{M} \approx 13.2$. The initial entropy of each of the periodic cells is $S = 1.5[0.5\ln(1.5)] + 0.125\ln(1.5 \times 0.0125)] = -0.4415$.

For our 1D code, we continued to use the classical AV (see Eq. (11)) with parameters $\alpha = \beta = 1$ and $\eta^2 = 0.05$. We used 2500 particles and constant (in time) smoothing lengths h_i, chosen such that the particles have 16 neighbors initially. Figure 17 shows a comparison between our 1D SPH code (dotted curve) and the quasi-analytic solution (solid curve) at a time $t = 0.15$. As expected, the 1D code does smooth out discontinuities in the density over a width of a few smoothing lengths. However, the agreement between the 1D code and the quasi-analytic solution is still very good.

As in the low Mach number case, we can compare the results from the 3D code to that of the 1D code, in order to evaluate the amount of spurious mixing and to determine the acceptable range of values for the AV parameters for our 3D calculations. Table III is the high Mach number equivalent of Table I. These 3D calculations employ $N = 10^4$ particles each with $N_N = 64$ neighbors, as in the 3D low Mach number calculations.

In Fig. 18 we present the results of 3D high Mach number shock-tube calculations for various α and β with the classical AV. For all the 3D calculations in this figure, we chose $\eta^2 = 0.01$ and used the Monaghan timestep routine with $C_N = 0.8$. The solid line is the result of the 1D calculation. It is apparent that the spurious displacement is smaller for stronger AV, as expected and as in the low Mach number tests. As also seen in the low Mach number tests, the case with the lowest spurious mixing ($\alpha = 5$, $\beta = 0$) has the worst fit to the energy curve of the 1D calculation. Therefore, the best choice of AV parameters will depend on the particular situation which is to be modeled. If spurious mixing is important to

TABLE III

High Mach Number Shock-Tube Cases with $\gamma = 5/3$

AV routine	α	β	dt routine	C_N	Steps to $t = 1$	Steps to $t = 4$	$\Delta E/E$ at $t = 4$	$\delta_y^2 + \delta_z^2$ $[n^{-2/3}]$ at $t = 4$	$\Delta(U/E)_{\max}$	$\Delta S_{\max}$
None			M	0.3	97	376	0.04%	300.1	0.207	0.85
C	0	1	M	0.1	411	1512	0.02%	6.02	0.028	0.11
C	0	1	M	0.8	83	247	1.49%	5.46	0.026	0.12
C	0	5	M	0.8	124	371	1.82%	1.39	0.065	0.14
C	0.1	1	M	0.3	227	687	0.07%	3.84	0.024	0.096
C	0.2	0.5	M	0.3	206	682	0.05%	4.57	0.027	0.14
C	0.2	1	M	0.3	231	715	0.06%	2.85	0.024	0.089
C	0.2	1.25	M	0.3	238	730	0.12%	2.27	0.027	0.084
C	0.3	1	M	0.3	233	746	0.06%	2.13	0.025	0.085
C	0.3	1.25	M	0.3	243	763	0.12%	1.76	0.028	0.081
C	0.5	1	M	0.3	245	827	0.05%	1.38	0.027	0.079
C	0.5	1.25	M	0.3	252	830	0.10%	1.26	0.031	0.075
C	0.5	2.5	M	0.3	283	896	0.16%	1.06	0.046	0.063
C	0.7	1.5	M	0.3	268	936	0.08%	0.94	0.037	0.068
C	1	0	M	0.8	97	386	0.71%	1.16	0.027	0.127
C	1	1	M	0.8	106	389	0.27%	0.85	0.033	0.076
C	1	1.5	M	0.3	292	1058	0.05%	0.82	0.042	0.062
C	1	2	M	0.3	299	1057	0.08%	0.79	0.048	0.063
C	1	2	M	0.8	112	397	0.02%	0.80	0.045	0.069
C	2	2	M	0.8	146	557	0.04%	0.56	0.059	0.089
C	5	0	M	0.8	258	1039	0.08%	0.27	0.077	0.12
HK	0	1.25	M	0.3	131	494	0.28%	9.71	0.053	0.072
HK	0.2	0.5	M	0.3	144	555	0.33%	13.41	0.043	0.086
HK	0.5	0.5	M	0.3	186	727	0.11%	4.04	0.041	0.080
HK	0.5	1	M	0.3	180	698	0.08%	2.78	0.060	0.066
HK	1	0	M	0.3	249	976	0.08%	2.90	0.029	0.11
HK	1	0.25	M	0.3	251	979	0.04%	2.26	0.046	0.082
HK	1	1	S	0.8	44	163	3.20%	1.62	0.069	0.093
HK	1	1	M	0.3	238	941	0.02%	1.57	0.073	0.083
HK	1	1	M	0.8	89	350	0.08%	1.55	0.068	0.077
B	0	$2.5 \times \gamma/2$	M	0.3	279	834	0.31%	8.25	0.030	0.077
B	$0.2 \times \gamma/2$	$0.5 \times \gamma/2$	M	0.3	194	664	0.10%	16.99	0.055	0.19
B	$0.5 \times \gamma/2$	$0.75 \times \gamma/2$	M	0.3	243	854	0.02%	5.35	0.029	0.13
B	$0.5 \times \gamma/2$	$1 \times \gamma/2$	M	0.3	254	857	0.02%	4.35	0.025	0.11
B	$1 \times \gamma/2$	$0.75 \times \gamma/2$	M	0.3	293	1076	0.02%	1.88	0.024	0.089
B	$1 \times \gamma/2$	$1 \times \gamma/2$	M	0.3	300	1106	0.02%	1.57	0.026	0.074
B	$1 \times \gamma/2$	$1 \times \gamma/2$	M	0.8	112	413	0.33%	1.62	0.024	0.080
B	$1 \times \gamma/2$	$1.25 \times \gamma/2$	M	0.3	301	1077	0.03%	1.45	0.028	0.068
B	$1 \times \gamma/2$	$1.5 \times \gamma/2$	M	0.3	306	1080	0.05%	1.40	0.031	0.066
B	$1 \times \gamma/2$	$2 \times \gamma/2$	M	0.3	316	1100	0.09%	1.29	0.037	0.064
B	$2 \times \gamma/2$	0	M	0.3	403	1617	0.03%	0.91	0.030	0.065
B	$2 \times \gamma/2$	$1 \times \gamma/2$	M	0.3	405	1577	0.00%	0.79	0.041	0.058
B	$2 \times \gamma/2$	$1.25 \times \gamma/2$	M	0.3	406	1562	0.01%	0.81	0.043	0.063

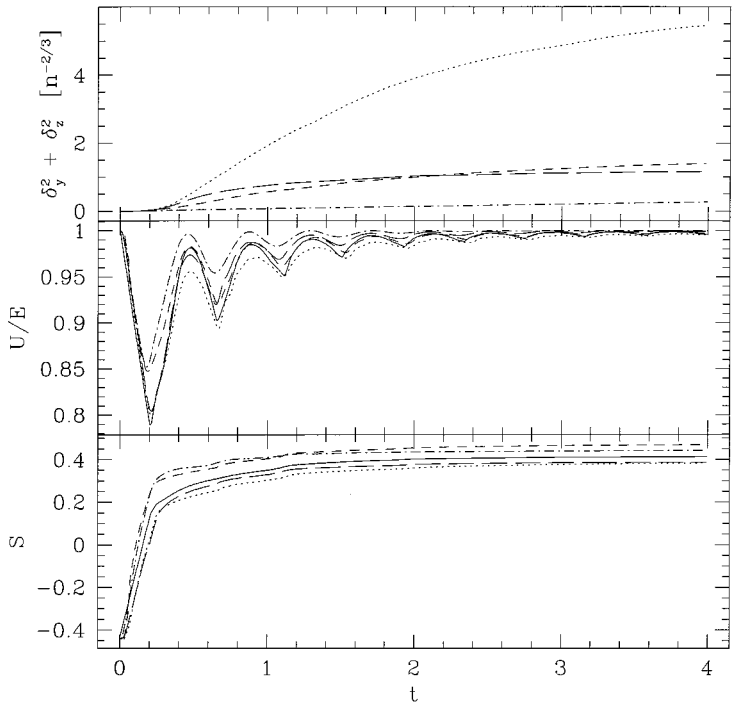

FIG. 18. Dependence of the high Mach number shock-tube calculations on the AV parameters α and β for the classical AV and our 3D SPH code. The different lines represent different values, as follows: $\alpha = 0$, $\beta = 1$ (dotted curve); $\alpha = 0$, $\beta = 5$ (short dashed curve); $\alpha = 1$, $\beta = 0$ (long dashed curve); $\alpha = 5$, $\beta = 0$ (dot-dash). The solid curve is the result of the 1D calculation presented in Fig. 17.

control, then a strong viscosity is favorable. On the other hand, if spurious mixing is not an issue, one could use a weaker AV to more accurately determine the evolution of the system.

Figure 19 shows, as a function of time, the average square displacement perpendicular to the bulk fluid flow $\delta_y^2 + \delta_z^2$, the ratio of internal to total energy U/E, and the entropy S for three calculations with different forms of AV: the classical AV with $\alpha = 0.5$, $\beta = 1$ (long dashed curve), the HK AV with $\alpha = \beta = 0.5$ (short dashed curve), and the Balsara AV with $\alpha = \beta = \gamma/2$ (dotted curve). In the bottom two frames, the solid curve corresponds to our 1D SPH code. As will be discussed in Subsection 7.4, these choices for α and β are our recommended values. We see that the HK AV does allow slightly more spurious mixing and does not quite match the 1D code's U/E curve as well. Nevertheless, all three AV forms adequately treat the strong shocks of this system.

5.3. *High Mach Number Cases with $\gamma = 3$*

Of course, not all fluids are well-described by the ideal gas ($\gamma = 5/3$) approximation. For example, neutron star matter is best represented by a stiff equation of state with $\gamma \approx 2$–3, while an isothermal gas can be described with $\gamma = 1$. Changing the value of γ changes the thermodynamic properties of the material we model with SPH, which in turn affects the way the AV behaves. Therefore, to investigate the dependence on γ of the "optimal" AV parameters, we have performed some shock-tube calculations with $\gamma = 3$. The fluid slabs were set up to have the same Mach number as the previous high Mach number ideal gas

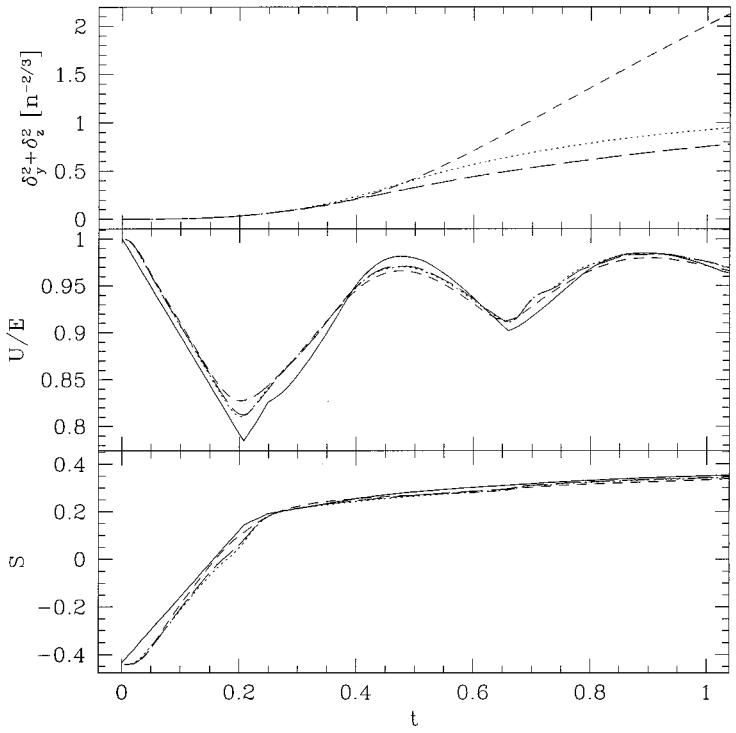

FIG. 19. The same situation as Fig. 16, but for our high Mach number shock-tube test.

tests ($\mathcal{M}=13.2$): $\rho_l=1$, $p_l=1$, $\rho_r=0.25$, and $p_r=8.78\times10^{-7}$. The initial entropy of each periodic cell is $S=0.5[0.5\ln(0.5)+0.125\ln(0.0562/2)]=-0.3965$.

For the corresponding calculation with the 1D code, we used the classical AV scheme with $\alpha=\beta=1$ and $\eta^2=0.05$, 2500 particles and 16 initial neighbors, as in the previous high Mach number case. For our 3D calculations, we used 10^4 particles with 64 initial neighbors, and a variety of AV parameters with all three AV schemes. We used the Monaghan timestep routine with $C_N=0.3$. A comparison between the 1D and 3D runs is given in Table IV, and a selection of the results is shown in Fig. 20.

As in the ideal gas case, spurious diffusion is smaller for stronger artificial viscosities. The calculations with small α show additional "wiggles" in the energy curve (see Fig. 20) and larger errors in energy conservation (see Table IV), suggesting the appearance of numerical instabilities for strong shocks treated by weak AV forms. In general, we find that the level of energy conservation is worse in our $\gamma=3$ calculations than in our $\gamma=5/3$ calculations (compare Tables III and IV).

6. SHEAR FLOWS

6.1. *Periodic Box Tests*

In order to model a shear flow of infinite extent, we return to a cubical box with a side length $L=1$ and periodic boundary conditions. The boundary conditions on the $x=\pm\frac{L}{2}$ and $z=\pm\frac{L}{2}$ faces are identical to the periodic boundary conditions in the simple box tests of Section 3: when a particle crosses one of these faces it is reinserted with the same velocity

TABLE IV
High Mach Number Shock-Tube Cases with $\gamma = 3$

AV routine	α	β	Steps to $t=1$	Steps to $t=4$	$\Delta E/E$ at $t=4$	$\delta_y^2+\delta_z^2$ $[n^{-2/3}]$ at $t=4$	$\Delta(U/E)_{\max}$	$\Delta S_{\max}$
C	0.2	0.5	238	849	1.10%	1.90	0.140	0.073
C	0.28	0.56	240	867	1.01%	1.27	0.114	0.065
C	0.3	1.0	248	877	0.63%	1.03	0.081	0.049
C	0.5	1.0	261	938	0.49%	0.79	0.045	0.039
C	0.5	1.25	264	939	0.37%	0.81	0.037	0.034
C	0.7	1.5	284	1013	0.26%	0.68	0.040	0.024
C	0.9	1.8	307	1106	0.20%	0.59	0.047	0.022
C	1.0	1.5	313	1147	0.24%	0.58	0.049	0.021
HK	0.2	0.5	184	708	1.30%	3.48	0.076	0.042
HK	0.28	0.28	223	880	0.54%	1.28	0.061	0.026
HK	0.5	0.5	216	844	0.62%	1.43	0.048	0.027
HK	0.5	1.0	214	836	0.48%	1.21	0.077	0.023
HK	0.7	0.5	243	955	0.40%	1.15	0.076	0.025
HK	0.9	0.9	269	1063	0.18%	0.83	0.115	0.037
B	$0.5\times\gamma/2$	$1.0\times\gamma/2$	271	1014	0.79%	1.35	0.094	0.060
B	$0.56\times\gamma/2$	$0.56\times\gamma/2$	286	1100	0.85%	1.41	0.103	0.068
B	$1.0\times\gamma/2$	$0.75\times\gamma/2$	329	1269	0.47%	0.83	0.039	0.042
B	$1.0\times\gamma/2$	$1.0\times\gamma/2$	326	1240	0.45%	0.82	0.031	0.038
B	$1.0\times\gamma/2$	$1.25\times\gamma/2$	324	1226	0.39%	0.81	0.033	0.035
B	$1.8\times\gamma/2$	$1.8\times\gamma/2$	421	1610	0.22%	0.60	0.066	0.018
B	$2.0\times\gamma/2$	$1.0\times\gamma/2$	446	1722	0.24%	0.56	0.066	0.018

at the corresponding position on the opposing face. On the $y=\pm\frac{L}{2}$ faces, however, we implement"slipping" boundary conditions in order to maintain a velocity field with a shear flow: if a particle crosses a face with a velocity (v_x, v_y, v_z) at a position $(x, \pm\frac{L}{2}, z)$, it is reinserted with a new velocity $(v_x \mp v_0, v_y, v_z)$ at the position $(x \mp v_0 t + kL, \mp\frac{L}{2}, z)$, where t is the time elapsed since the beginning of the calculation and k is the integer which places the particle in the central periodic cell. The resulting "stationary Couette flow" has a velocity field close to $(v_0 y/L, 0, 0)$ (see Fig. 21).

Neighbor searching across the $x=\pm\frac{L}{2}$ and $z=\pm\frac{L}{2}$ faces is done exactly as in Subsection 3.1. Across the $y=\pm\frac{L}{2}$ faces, the slipping boundary conditions are taken into account: the criterion for particle j having particle i as a neighbor is that there exists integers k, l, and m such that the position $(x_i + kL + l v_0 t, y_i + lL, z_i + mL)$ is within a distance $2h_j$ of (x_j, y_j, z_j). In addition, the relative velocity of particles interacting across the $y=\pm\frac{L}{2}$ boundaries is adjusted by v_0 when computing the AV term Π_{ij}. In this way, particle interactions across the boundaries behave identically to interactions within the box.

Our units of distance and mass are the length of the box and the total mass in the box: $L=1$ and $M=Nm\equiv 1$, where N is the number of particles. We set the entropy variable $A=1$ for all the particles initially. Consequently the unit of velocity in our calculations is $\gamma^{-1/2}c_s$, where c_s is the initial sound speed, and the unit of time is $\gamma^{1/2}L/c_s$.

Figure 22 shows the spurious square displacement, energies, and entropy as a function of time in three calculations with $N=1000$, $N_N=64$, $v_0=0.1\gamma^{-1/2}c_s$, and various forms of AV. The system was relaxed for the first 10 time units (without AV) towards a situation

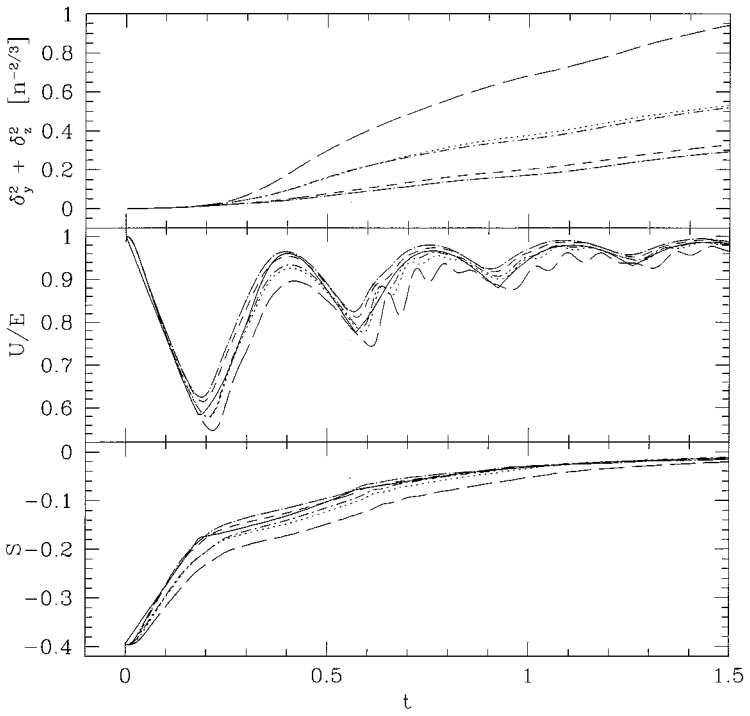

FIG. 20. The same situation as Fig. 16, but for the high Mach number shock-tube test with $\gamma = 3$. The solid line is for the 1D calculation, and the others are the results of the 3D calculations with the following AV schemes and parameters: dotted, $\alpha = 0.5$, $\beta = 1.0$, classical AV; short dash, $\alpha = 0.9$, $\beta = 1.8$, classical AV; long dash, $\alpha = 0.28$, $\beta = 0.56$, classical AV; dot-short dash, $\alpha = 1.0 \times \gamma/2$, $\beta = 1.0 \times \gamma/2$, Balsara AV; dot-long dash, $\alpha = 1.8 \times \gamma/2$, $\beta = 1.8 \times \gamma/2$, Balsara AV; short dash-long dash, $\alpha = 0.56 \times \gamma/2$, $\beta = 0.56 \times \gamma/2$, Balsara AV.

with $(v_x, v_y, v_z) = (v_0 y/L, 0, 0)$, while from $t = 10$ to 50 the system evolves freely with the slipping boundary conditions and AV.

Notice the increase in energy once the relaxational damping is turned off: roughly a 1% increase in E per time unit. This increase results from the slipping boundary conditions and, for a given AV form and AV parameters, is nearly independent of the resolution. Since we are moving the boundary surfaces by hand and since there is viscosity, there is a shear stress at the boundaries and work is being done on the system. This behavior is analogous to that of a truly viscous fluid forced to undergo shear flow between close moving boundaries (as in a viscosimeter): the added energy goes into heating the fluid.

Since the faces of our cubical box have surface area L^2, the viscous force F_x acting on the fluid inside of the $y = \pm L/2$ faces is

$$F_x = \pm\eta \frac{\partial v_x}{\partial y} L^2 = \pm\eta v_0 L, \tag{30}$$

where η is the dynamic viscosity (not to be confused with the AV parameter η^2). The rate of energy change of the system is therefore

$$\frac{dE}{dt} = [F_x v_x]_{y=-L/2} + [F_x v_x]_{y=+L/2} \tag{31}$$

$$= \eta v_0^2 L. \tag{32}$$

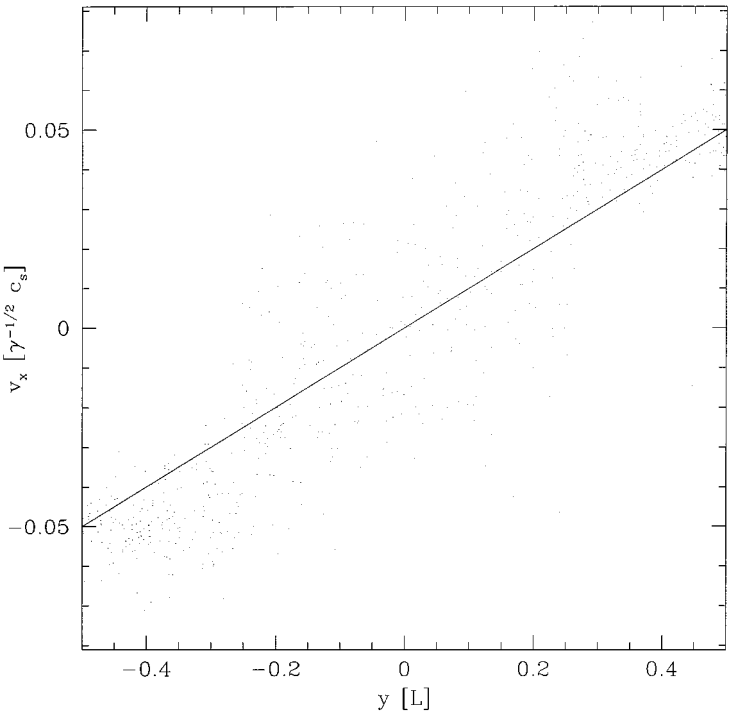

FIG. 21. Particle velocities in the x-direction plotted against their y coordinates. Slipping boundary conditions at $y = \pm\frac{1}{2}$ are used to maintain the shear flow. The system was relaxed without AV for the first 10 time units towards a configuration with $v_x = v_0 y/L$, $v_y = v_z = 0$ (the solid line), and then allowed to evolve with AV for another 10 time units to the state shown in this figure. Here $v_0 = 0.1 c_s \gamma^{-1/2}$, and $L = 1$ is the unit of length. We used $N = 1000$ particles each with $N_N = 64$ neighbors on average and the classical AV with $\alpha = 0.5$ and $\beta = 1$.

Measuring the rate of energy increase therefore allows us to numerically determine the dynamic viscosity. This procedure for measuring viscosity is also implemented in molecular dynamics (e.g., [58]). To calculate the kinematic viscosity ν from the dynamic viscosity η, one simply uses $\nu \equiv \eta/\rho = \eta N/(Mn)$, where n is the number density of particles.

In the absence of any spurious motion, SPH particles should maintain the same spatial coordinates y and z throughout the calculation. By monitoring motion in these two dimensions, we can therefore easily quantify the extent of spurious diffusion. As in Section 3, the square displacement increases linearly with time at late times. Here we measure the diffusion coefficient D by fitting the relation $3(\delta_y^2 + \delta_z^2)/2 = Dt$. In practice, we determine η and D from the average slope of the energy and square displacement curves, respectively, between times $t = 12$ and $t = 50$. Tables V and VI list the results of a set of runs at two different shear velocities with $N_N = 64$. We vary the AV scheme and the AV parameters, and monitor the time averaged velocity dispersion $\langle (v_y^2 + v_z^2)/c_s^2 \rangle$ between $t = 12$ and 50. We also list the viscosity η (as determined from Eq. (32)), the diffusion coefficient D, and the product ηD for each case (all converted into units $M = c_s = n = 1$ to keep our results applicable to general situations). In the last three columns, the number in parentheses ( ) is the error in the last digit, or last two digits, that is quoted. The uncertainties for the viscosity η and the diffusion coefficient D are determined from the root mean square deviation of $E(t)$ and of $\delta_y^2(t) + \delta_z^2(t)$ from the best-fit linear curve. In Table VII we present results from a

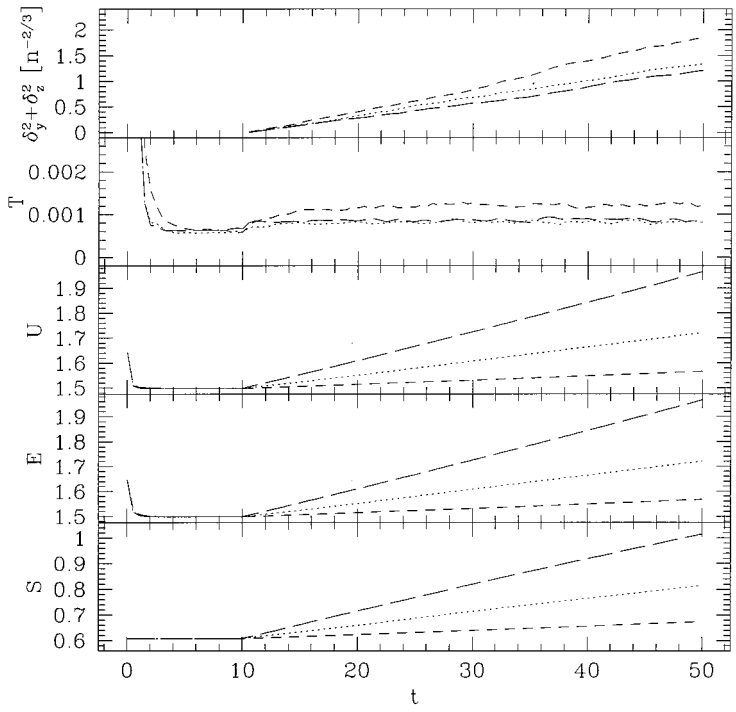

FIG. 22. The spurious square displacement in the direction perpendicular to the fluid flow, energies, and entropy as a function of time in three calculations of a shear flow using $N = 1000$ and $N_N = 64$ with different forms of AV: the classical AV with $\alpha = 0.5$, $\beta = 1$ (long dashed curve), the HK AV with $\alpha = \beta = 0.5$ (short dashed curve), and the Balsara AV with $\alpha = \beta = 1 \times \gamma/2$ (dotted curve). The system was relaxed for the first 10 time units towards a situation with $(v_x, v_y, v_z) = (0.1 c_s \gamma^{-1/2} y/L, 0, 0)$, while from $t = 10$ to 50 the system freely evolves with slipping boundary conditions.

handful of calculations with various neighbor numbers N_N. All of the calculations use constant smoothing lengths, as well as a constant timestep $dt = 0.01$ so that fixed computational resources are available.

6.2. *Rapidly Rotating, Self-gravitating Fluids*

Rotation plays an important role in many hydrodynamic processes in astrophysics. For instance, the collision of two stars typically results in a rapidly and differentially rotating merger remnant. AV tends to damp away any such differential rotation due to the relative velocity of neighboring particles at slightly different radii. In this section, we consider a differentially rotating, self-gravitating spheroid and analytically estimate the viscous timescale for each of the three AV forms examined in this paper. Our analytic estimates are then compared against numerical determinations of the viscous timescale. The larger the viscous timescale, the more closely the calculation is treating the gas as a perfect fluid.

As our concrete example, we consider an axisymmetric equilibrium configuration rotating with an angular velocity $\Omega \propto \varpi^{-\lambda}$, where the cylindrical radius ϖ is the distance to the rotation axis. In this case, the magnitude of the quantity $(\mathbf{v}_i - \mathbf{v}_j) \cdot (\mathbf{r}_i - \mathbf{r}_j)$ which appears in Eq. (12) is $\sim h \Delta v$ for two neighboring particles separated by $\sim h$, a typical smoothing length, where the shear velocity $\Delta v \equiv \lambda \Omega h$. Note that $\Delta v = 0$ for the special case of rigid rotation ($\lambda = 0$).

TABLE V

$N = 1000$, $N_N = 64$, $v_0/c_s = 0.1\gamma^{-1/2}$, $\gamma = 5/3$, $dt = 0.01$ Shear Tests

AV routine	α	β	$\langle(v_y^2+v_z^2)/c_s^2\rangle^{1/2}$	$\eta[Mc_sn^{2/3}]$	$D[c_sn^{-1/3}]$	$\eta D[Mc_s^2n^{1/3}]$
None			0.337	$3.0(1)\times10^{-4}$	2.85(6)	$8.4(4)\times10^{-4}$
C	0.0	1.00	0.020	$1.332(1)\times10^{-3}$	$4.59(5)\times10^{-3}$	$6.13(7)\times10^{-6}$
C	0.0	2.50	0.016	$2.763(5)\times10^{-3}$	$3.89(4)\times10^{-3}$	$1.07(1)\times10^{-5}$
C	0.0	10.00	0.012	$8.71(3)\times10^{-3}$	$3.73(7)\times10^{-3}$	$3.25(7)\times10^{-5}$
C	0.3	0.50	0.013	$5.60(4)\times10^{-3}$	$3.91(5)\times10^{-3}$	$2.19(3)\times10^{-5}$
C ($\eta^2=0.002$)	0.3	1.00	0.013	$6.16(6)\times10^{-3}$	$3.51(3)\times10^{-3}$	$2.16(3)\times10^{-5}$
C	0.3	1.00	0.013	$6.05(5)\times10^{-3}$	$3.53(7)\times10^{-3}$	$2.14(5)\times10^{-5}$
C ($\eta^2=0.05$)	0.3	1.00	0.013	$5.71(4)\times10^{-3}$	$3.95(4)\times10^{-3}$	$2.26(3)\times10^{-5}$
C	0.5	1.00	0.012	$9.09(10)\times10^{-3}$	$3.53(7)\times10^{-3}$	$3.21(7)\times10^{-5}$
C	0.8	1.25	0.012	$1.37(3)\times10^{-2}$	$3.78(6)\times10^{-3}$	$5.2(1)\times10^{-5}$
C	1.0	1.00	0.012	$1.64(4)\times10^{-2}$	$3.68(4)\times10^{-3}$	$6.0(1)\times10^{-5}$
C	1.0	1.25	0.012	$1.66(3)\times10^{-2}$	$3.44(9)\times10^{-3}$	$5.7(2)\times10^{-5}$
C	2.0	0.00	0.010	$3.1(1)\times10^{-2}$	$3.7(1)\times10^{-3}$	$1.12(5)\times10^{-4}$
C	3.0	0.00	0.009	$4.8(2)\times10^{-2}$	$3.57(3)\times10^{-3}$	$1.71(8)\times10^{-4}$
HK	0.0	1.25	0.082	$1.72(5)\times10^{-4}$	0.17(4)	$3.0(7)\times10^{-5}$
HK	0.0	10.00	0.038	$5.08(4)\times10^{-4}$	$2.1(5)\times10^{-2}$	$1.1(3)\times10^{-5}$
HK	0.1	0.50	0.066	$4.15(2)\times10^{-4}$	0.11(4)	$4.5(17)\times10^{-5}$
HK	0.5	0.50	0.024	$1.34(1)\times10^{-3}$	$5.4(1)\times10^{-3}$	$7.3(2)\times10^{-6}$
HK	0.5	1.00	0.025	$1.39(3)\times10^{-3}$	$5.32(15)\times10^{-3}$	$7.4(3)\times10^{-6}$
HK	1.0	1.00	0.022	$2.64(3)\times10^{-3}$	$5.05(13)\times10^{-3}$	$1.33(4)\times10^{-5}$
B	$0.0\times\gamma/2$	$1.00\times\gamma/2$	0.026	$2.72(1)\times10^{-4}$	$1.16(3)\times10^{-2}$	$3.13(7)\times10^{-6}$
B	$0.0\times\gamma/2$	$2.50\times\gamma/2$	0.023	$4.53(1)\times10^{-4}$	$7.0(1)\times10^{-3}$	$3.20(7)\times10^{-6}$
B	$0.0\times\gamma/2$	$10.00\times\gamma/2$	0.020	$1.055(3)\times10^{-3}$	$5.8(1)\times10^{-3}$	$6.1(1)\times10^{-6}$
B ($\eta^2=0.002$)	$0.5\times\gamma/2$	$0.50\times\gamma/2$	0.013	$2.33(2)\times10^{-3}$	$4.0(2)\times10^{-3}$	$9.3(5)\times10^{-6}$
B	$0.5\times\gamma/2$	$1.00\times\gamma/2$	0.018	$2.25(1)\times10^{-3}$	$3.42(35)\times10^{-3}$	$7.7(8)\times10^{-6}$
B	$1.0\times\gamma/2$	$0.00\times\gamma/2$	0.015	$4.22(3)\times10^{-3}$	$3.15(17)\times10^{-3}$	$1.33(7)\times10^{-5}$
B	$1.0\times\gamma/2$	$1.00\times\gamma/2$	0.015	$4.33(2)\times10^{-3}$	$3.93(5)\times10^{-3}$	$1.70(3)\times10^{-5}$
B	$1.0\times\gamma/2$	$2.00\times\gamma/2$	0.014	$4.444(7)\times10^{-3}$	$4.15(8)\times10^{-3}$	$1.84(3)\times10^{-5}$
B	$2.0\times\gamma/2$	$0.00\times\gamma/2$	0.013	$8.5(1)\times10^{-3}$	$3.69(5)\times10^{-3}$	$3.13(5)\times10^{-5}$
B	$3.0\times\gamma/2$	$0.00\times\gamma/2$	0.012	$1.584(25)\times10^{-2}$	$3.82(6)\times10^{-3}$	$6.0(1)\times10^{-5}$

If the AV is of the form of Eq. (11) with $\beta = 0$, Eq. (26) gives $\dot{v}^{\rm AV}$ and the viscous dissipation timescale $\tau \equiv v/\dot{v}^{\rm AV} = \Omega\varpi/\dot{v}^{\rm AV} \sim \varpi N_N^{1/2}/(\alpha\lambda c_s)$. Note that this timescale τ is not directly dependent on N: increasing N while keeping N_N fixed would not therefore affect the viscous timescale in this case. For general α and β, we analytically estimate from Eq. (11) that

$$\Pi_{ij} \approx -j_1\frac{\alpha\Delta v c_s}{\rho} - j_2\frac{\beta\Delta v^2}{\rho} \qquad \text{(Classical AV)}, \tag{33}$$

where j_1 and j_2 are dimensionless coefficients of order unity. In this case Eq. (26) must be replaced by $\dot{v}^{\rm AV} \approx k_1\alpha c_s\,\Delta v/(hN_N^{1/2}) + k_2\beta\Delta v^2/(hN_N^{1/2})$, and the viscous timescale $\tau = v/\dot{v}^{\rm AV}$ is then given by

$$\tau \equiv \frac{v}{\dot{v}^{\rm AV}} \approx v\left(k_1\frac{\alpha\Delta v c_s}{hN_N^{1/2}} + k_2\frac{\beta\Delta v^2}{hN_N^{1/2}}\right)^{-1} = \left(k_1\frac{\alpha\lambda c_s}{\varpi N_N^{1/2}} + k_2\frac{\beta\lambda\Delta v}{\varpi N_N^{1/2}}\right)^{-1} \qquad \text{(Classical AV)}, \tag{34}$$

TABLE VI

$N = 1000$, $N_N = 64$, $v_0/c_s = 0.5\gamma^{-1/2}$, $\gamma = 5/3$, $dt = 0.01$ Shear Tests

AV routine	α	β	$\langle(v_y^2+v_z^2)/c_s^2\rangle^{1/2}$	$\eta[Mc_sn^{2/3}]$	$D[c_sn^{-1/3}]$	$\eta D[Mc_s^2n^{1/3}]$
None			0.128	$4.8(4)\times10^{-5}$	0.38(7)	$1.8(4)\times10^{-5}$
C	0.2	0.75	0.029	$9.3(6)\times10^{-3}$	$2.2(2)\times10^{-2}$	$2.1(2)\times10^{-4}$
C ($\eta^2=0.002$)	0.3	1.00	0.026	$1.5(1)\times10^{-2}$	$2.0(1)\times10^{-2}$	$3.0(3)\times10^{-4}$
C	0.3	1.00	0.026	$1.5(1)\times10^{-2}$	$2.0(1)\times10^{-2}$	$2.9(3)\times10^{-4}$
C ($\eta^2=0.05$)	0.3	1.00	0.026	$1.3(1)\times10^{-2}$	$2.1(2)\times10^{-2}$	$2.9(3)\times10^{-4}$
C	0.3	0.50	0.028	$1.19(10)\times10^{-2}$	$2.1(1)\times10^{-2}$	$2.4(3)\times10^{-4}$
C	0.4	0.50	0.026	$1.6(2)\times10^{-2}$	$1.9(2)\times10^{-2}$	$3.1(4)\times10^{-4}$
C	0.5	0.50	0.024	$2.2(2)\times10^{-2}$	$2.0(1)\times10^{-2}$	$4.3(5)\times10^{-4}$
C	0.5	1.00	0.023	$2.5(2)\times10^{-2}$	$1.8(1)\times10^{-2}$	$4.5(6)\times10^{-4}$
C	0.8	1.25	0.019	$4.5(5)\times10^{-2}$	$1.7(1)\times10^{-2}$	$7.5(10)\times10^{-4}$
C	1.0	0.25	0.019	$5.4(7)\times10^{-2}$	$1.59(7)\times10^{-2}$	$8.5(12)\times10^{-4}$
HK	0.0	1.25	0.079	$2.66(5)\times10^{-4}$	0.15(1)	$4.0(3)\times10^{-5}$
HK	0.0	10.00	0.063	$1.65(1)\times10^{-3}$	$7.3(4)\times10^{-2}$	$1.21(7)\times10^{-4}$
HK	0.1	0.50	0.069	$3.91(5)\times10^{-4}$	0.106(4)	$4.1(2)\times10^{-5}$
HK	0.2	0.50	0.062	$6.69(7)\times10^{-4}$	$7.3(3)\times10^{-2}$	$4.9(2)\times10^{-5}$
HK	0.2	0.75	0.061	$7.11(8)\times10^{-4}$	$6.8(3)\times10^{-2}$	$4.9(2)\times10^{-5}$
HK	0.3	0.50	0.059	$9.7(2)\times10^{-4}$	$5.8(3)\times10^{-2}$	$5.6(4)\times10^{-5}$
HK	0.4	0.50	0.056	$1.28(3)\times10^{-3}$	$5.4(5)\times10^{-2}$	$6.9(7)\times10^{-5}$
HK	0.5	0.50	0.055	$1.66(6)\times10^{-3}$	$5.5(4)\times10^{-2}$	$9.2(8)\times10^{-5}$
HK	0.8	1.25	0.052	$2.8(1)\times10^{-3}$	$4.6(7)\times10^{-2}$	$1.3(2)\times10^{-4}$
HK	1.0	0.25	0.051	$3.7(2)\times10^{-3}$	$4.4(6)\times10^{-2}$	$1.6(2)\times10^{-4}$
B	$0.0\times\gamma/2$	$1.00\times\gamma/2$	0.054	$5.90(4)\times10^{-4}$	$5.3(3)\times10^{-2}$	$3.1(2)\times10^{-5}$
B	$0.0\times\gamma/2$	$2.50\times\gamma/2$	0.045	$1.245(9)\times10^{-3}$	$3.1(3)\times10^{-2}$	$3.8(4)\times10^{-5}$
B	$0.0\times\gamma/2$	$10.00\times\gamma/2$	0.036	$4.10(2)\times10^{-3}$	$2.87(6)\times10^{-2}$	$1.18(3)\times10^{-4}$
B ($\eta^2=0.002$)	$0.5\times\gamma/2$	$0.50\times\gamma/2$	0.036	$3.8(2)\times10^{-3}$	$2.3(3)\times10^{-2}$	$8.7(10)\times10^{-5}$
B ($\eta^2=0.05$)	$0.5\times\gamma/2$	$0.50\times\gamma/2$	0.037	$3.6(2)\times10^{-3}$	$2.2(3)\times10^{-2}$	$7.8(13)\times10^{-5}$
B	$0.5\times\gamma/2$	$1.00\times\gamma/2$	0.036	$4.1(2)\times10^{-3}$	$2.4(2)\times10^{-2}$	$9.6(11)\times10^{-5}$
B	$0.8\times\gamma/2$	$1.25\times\gamma/2$	0.032	$7.1(4)\times10^{-3}$	$2.3(2)\times10^{-2}$	$1.6(2)\times10^{-4}$
B	$1.0\times\gamma/2$	$0.00\times\gamma/2$	0.031	$8.9(6)\times10^{-3}$	$2.2(2)\times10^{-2}$	$2.0(2)\times10^{-4}$
B	$1.0\times\gamma/2$	$0.75\times\gamma/2$	0.030	$9.2(6)\times10^{-3}$	$2.1(2)\times10^{-2}$	$1.9(2)\times10^{-4}$
B	$1.0\times\gamma/2$	$1.00\times\gamma/2$	0.030	$9.6(7)\times10^{-3}$	$2.0(3)\times10^{-2}$	$2.0(3)\times10^{-4}$
B	$1.0\times\gamma/2$	$1.25\times\gamma/2$	0.030	$9.5(6)\times10^{-3}$	$2.2(2)\times10^{-2}$	$2.1(3)\times10^{-4}$
B	$1.0\times\gamma/2$	$2.00\times\gamma/2$	0.030	$9.9(6)\times10^{-3}$	$2.2(2)\times10^{-2}$	$2.2(2)\times10^{-4}$
B	$2.0\times\gamma/2$	$0.00\times\gamma/2$	0.024	$2.5(2)\times10^{-2}$	$2.0(2)\times10^{-2}$	$4.9(7)\times10^{-4}$

TABLE VII

$N = 1000$, $v_0/c_s = 0.1\gamma^{-1/2}$, $\gamma = 5/3$, $dt = 0.01$ Shear Tests

AV routine	α	β	N_N	$\langle(v_y^2+v_z^2)/c_s^2\rangle^{1/2}$	$\eta[Mc_sn^{2/3}]$	$D[c_sn^{-1/3}]$	$\eta D[Mc_s^2n^{1/3}]$
B	$0.0\times\gamma/2$	$1.00\times\gamma/2$	20	0.060	$6.63(7)\times10^{-4}$	$7.0(3)\times10^{-3}$	$4.7(2)\times10^{-6}$
B	$0.0\times\gamma/2$	$1.00\times\gamma/2$	32	0.037	$2.98(2)\times10^{-4}$	$6.7(2)\times10^{-3}$	$2.00(7)\times10^{-6}$
B	$0.0\times\gamma/2$	$1.00\times\gamma/2$	64	0.026	$2.72(1)\times10^{-4}$	$1.16(3)\times10^{-2}$	$3.13(7)\times10^{-6}$
B	$1.0\times\gamma/2$	$0.00\times\gamma/2$	20	0.027	$4.85(3)\times10^{-3}$	$5.5(2)\times10^{-3}$	$2.67(10)\times10^{-5}$
B	$1.0\times\gamma/2$	$0.00\times\gamma/2$	48	0.017	$4.48(2)\times10^{-3}$	$3.85(8)\times10^{-3}$	$1.72(4)\times10^{-5}$
B	$1.0\times\gamma/2$	$0.00\times\gamma/2$	64	0.015	$4.22(3)\times10^{-3}$	$3.2(2)\times10^{-3}$	$1.33(7)\times10^{-5}$
B	$1.0\times\gamma/2$	$1.00\times\gamma/2$	20	0.026	$4.92(4)\times10^{-3}$	$5.16(8)\times10^{-3}$	$2.54(5)\times10^{-5}$
B	$1.0\times\gamma/2$	$1.00\times\gamma/2$	64	0.015	$4.33(2)\times10^{-3}$	$3.93(5)\times10^{-3}$	$1.70(3)\times10^{-5}$

where k_1 and k_2 are dimensionless coefficients of order unity. The ratio of the two terms on the right hand side of Eq. (34) tells us that the von Neumann–Richtmyer viscosity (corresponding to the term with β) yields a timescale longer than that of the bulk viscosity by a factor of $\sim \alpha c_s/(\beta \Delta v)$. The bulk viscosity therefore dominates the shear for the classical AV, provided only that $\Delta v \ll c_s$.

If the AV is instead given by HK form (Eq. (13)), dimensional analysis gives

$$\Pi_{ij} \approx -j_1' \frac{\alpha \Delta v c_s}{\rho N_N^{1/2}} - j_2' \frac{\beta \Delta v^2}{\rho N_N} \qquad \text{(HK AV)} \tag{35}$$

if $(\nabla \cdot \mathbf{v})_i$ or $(\nabla \cdot \mathbf{v})_j$ is negative (otherwise $\Pi_{ij} = 0$). Although our idealized velocity field satisfies $(\nabla \cdot \mathbf{v})_i = 0$, the numerical estimation of the velocity divergence, as computed by Eq. (15), gives small but non-zero results. In deriving Eq. (35) we have used $|(\mathbf{v}_i - \mathbf{v}_j) \cdot \nabla_i W_{ij}|/n \sim \Delta v/(h N_N)$, which implies $|\nabla \cdot \mathbf{v}|_i \sim \Delta v/(h N_N^{1/2})$ from Eq. (15). Before we can estimate $\dot{v}_i^{\rm AV} \equiv |-\sum_j m_j \Pi_{ij} \nabla_i W_{ij}|$ we must note that the summation $-\sum_j m_j \Pi_{ij} \nabla_i W_{ij}$ appearing in Eq. (10) scales like the number of terms N_N in the summation (*not* $N_N^{1/2}$ as with the classical AV): the condition $(\nabla \cdot \mathbf{v})_i < 0$ in Eq. (14) requires that the vectors $\nabla_i W_{ij}$ for which $\Pi_{ij} \neq 0$ are found preferentially in the direction of particle i's velocity deviation from the local fluid flow. Therefore, $\dot{v}^{\rm AV} \approx k_1' \alpha c_s \, \Delta v/(h N_N^{1/2}) + k_2' \beta \Delta v^2/(h N_N)$, and the timescale satisfies

$$\tau \equiv \frac{v}{\dot{v}^{\rm AV}} \approx v \left(k_1' \frac{\alpha c_s \, \Delta v}{h N_N^{1/2}} + k_2' \frac{\beta \Delta v^2}{h N_N} \right)^{-1} = \left(k_1' \frac{\alpha \lambda c_s}{\varpi N_N^{1/2}} + k_2' \frac{\beta \lambda \, \Delta v}{\varpi N_N} \right)^{-1} \qquad \text{(HK AV)}, \tag{36}$$

where j_1', j_2', k_1', and k_2' are coefficients of order unity.

Comparing Eqs. (34) and (36) we see that the timescale due to the bulk viscosity is of the same order of magnitude for the classical and HK artificial viscosities; however, the timescale associated with the von Neumann–Richtmyer term is longer in the HK AV by a factor $N_N^{1/2}$. Since typical 3D calculations have $N_N \sim 50$–100, the increase in the viscous dissipation timescale is substantial whenever von Neumann–Richtmyer viscosity terms are significant.

If the AV is given by Balsara's form (Eq. (16)), we need to estimate the size of f_i (Eq. (18)) before we can estimate Π_{ij}. For our assumed velocity field $|\nabla \times \mathbf{v}| = (2 - \lambda)\Omega$. Therefore, provided that λ is far enough from 2 that the curl of the velocity dominates over the other terms in the denominator on the right hand side of Eq. (18), an SPH evaluation of f_i gives

$$f_i \approx \frac{|\nabla \cdot \mathbf{v}|_i}{|\nabla \times \mathbf{v}|_i} \sim \frac{\lambda}{N_N^{1/2}(2 - \lambda)} \equiv f. \tag{37}$$

Recalling that $(p_i/\rho_i^2 + p_j/\rho_j^2) \approx 2c_s^2/(\gamma \rho)$, we estimate from Eq. (16) that

$$\Pi_{ij} \approx -j_1'' \frac{\alpha \Delta v c_s}{\rho} \left(\frac{2}{\gamma} f \right) - j_2'' \frac{\beta \Delta v^2}{\rho} \left(\frac{2}{\gamma} f^2 \right) \qquad \text{(Balsara AV)}, \tag{38}$$

where j_1'' and j_2'' are coefficients of order unity. Therefore, $\dot{v}^{\rm AV} \approx 2k_1''\alpha c_s\,\Delta v f/(\gamma h N_N^{1/2}) + 2k_2''\beta\Delta v^2 f^2/(\gamma h N_N^{1/2})$, and the viscous timescale is given by

$$\tau \equiv \frac{v}{\dot{v}^{\rm AV}} \approx v\left[k_1''\frac{\alpha\Delta v c_s}{h N_N^{1/2}}\left(\frac{2}{\gamma}f\right) + k_2''\frac{\beta\,\Delta v^2}{h N_N^{1/2}}\left(\frac{2}{\gamma}f^2\right)\right]^{-1}$$

$$\approx \left[k_1''\frac{\alpha\lambda^2 c_s}{\varpi N_N(2-\lambda)}\frac{2}{\gamma} + k_2''\frac{\beta\lambda^3\,\Delta v}{\varpi N_N^{3/2}(2-\lambda)^2}\frac{2}{\gamma}\right]^{-1} \qquad \text{(Balsara AV)}, \qquad (39)$$

where k_1'' and k_2'' are also coefficients of order unity.

To test these simple analytic estimates we computed $\tau_i = v_i/|-\sum_j m_j\Pi_{ij}\nabla_i W_{ij}|$ for a rapidly and differentially rotating spheroid. This spheroid was constructed in three steps: (1) we created a spherical $n=3$, $\Gamma_1 = 5/3$ configuration (pressure profile $p = A\rho^{5/3} \propto \rho^{4/3}$, and consequently $A \propto \rho^{-1/3}$) of radius R and mass M; (2) assigned a velocity $v_0 = 0.5$ (in units where $G = M = R = 1$) in the azimuthal direction $\hat{\phi}$ to all particles; and (3) relaxed to a rotating equilibrium state by means of an artificial "drag" force $\propto v_0\hat{\phi} - \mathbf{v}_i$ on the particles. The resulting rapidly rotating spheroid ($T/|W| \approx 0.11$) is in virial equilibrium with a rotation profile close to $\Omega \propto \varpi^{-1}$. At small ϖ, when the particle smoothing kernels overlap with the rotation axis, the finite resolution of the SPH scheme cause deviations from the $\Omega \propto \varpi^{-1}$, cutting off the divergence of Ω at $\varpi = 0$. The centrifugal force near $\varpi = 0$ nevertheless is strong enough to make the density a local minimum there; in the equatorial plane the maximum density actually occurs at $\varpi \approx 0.14$.

For such a configuration modeled using $N = 10^4$ and $N_N \approx 64$, Fig. 23 compares the actual timescale $\tau_i = v_i/|-\sum_j m_j\Pi_{ij}\nabla_i W_{ij}|$ computed directly from the SPH code (left frame) against our analytic estimates (right frame): (a) classical AV with $\alpha = 1$, $\beta = 0$; (b) classical AV with $\alpha = 0$, $\beta = 1.5$; (c) HK AV with $\alpha = 0.5$, $\beta = 0$; (d) HK AV with $\alpha = 0$, $\beta = 0.5$; (e) Balsara AV with $\alpha = \gamma/2$, $\beta = 0$; and (f) Balsara AV with $\alpha = 0$, $\beta = 1.5 \times \gamma/2$. For all six cases, the same set of particles are analyzed, with the only difference being the way $\dot{v}_i^{\rm AV}$ is calculated. It is clear that our analytic estimates do a good job of reproducing the overall trend in position and magnitude of the actual timescale τ. The estimates for cases (a) and (c) are identical, while the average measured timescale in case (a) is slightly less than that of case (c), which implies $k_1' < k_1$. For each of the AV forms, the timescale due to the bulk viscosity is significantly less than that due to the von Neumann–Richtmyer viscosity.

Our analytic estimates of Π_{ij} and the viscous dissipation timescale τ have neglected the effects of additional velocity contributions due to particle noise. For this reason, the numerical coefficients in Eqs. (34), (36), and (39) are not strictly constant but instead have some complicated dependence on the neighbor number N_N and noise level in the system. Consequently when the particle noise is comparable to the shear velocity, our expressions tend to overestimate the timescale. Figure 24 shows the timescales in 6 different calculations which have evolved freely for 1 time unit from the relaxed particle state of Fig. 23. During this evolution, the particle noise level grows large enough to make our analytic formulae overestimate the timescale for cases (d), (e), and (f) by a factor of $\sim$2. Furthermore, while both the HK and Balsara AVs continue to have significantly longer timescales than the classical AV, the timescale for the Balsara AV is now only slightly larger than for the HK AV.

Figure 25 shows the evolution of the angular momentum profile Ω in seven different calculations which began with the same initial conditions but implemented the different

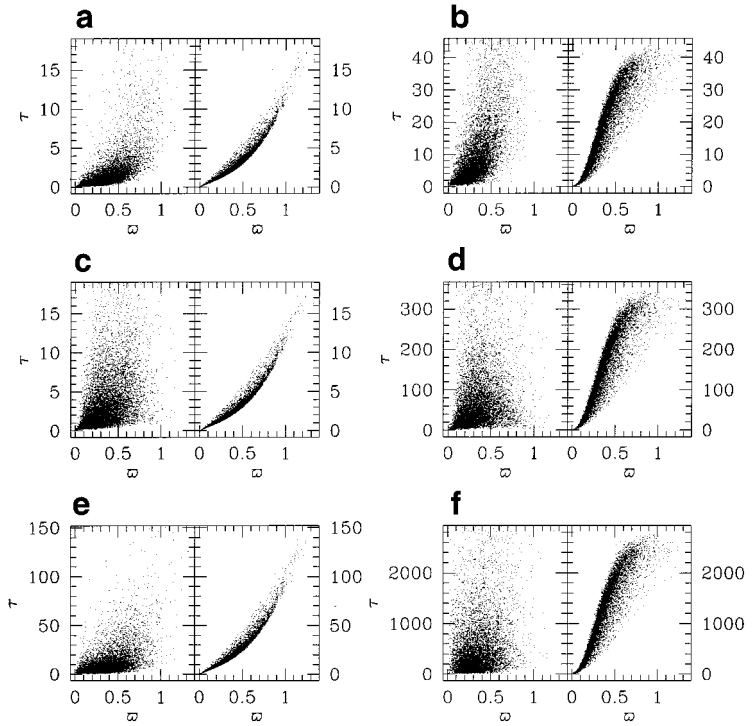

FIG. 23. The viscous timescale as a function of the distance ϖ from the rotation axis for various artificial viscosities in a system which has been relaxed into a rapidly, differentially rotating configuration: (a) $\alpha = 2$ and $\beta = 0$ in Eq. (11); (b) $\alpha = 0$ and $\beta = 2$ in Eq. (11); (c) $\alpha = 2$ and $\beta = 0$ in Eq. (13); (d) $\alpha = 0$ and $\beta = 2$ in Eq. (13); (e) $\alpha = 2 \times \gamma/2$ and $\beta = 0$ in Eq. (16); and (f) $\alpha = 0$ and $\beta = 2 \times \gamma/2$ in Eq. (16). Both the actual timescale $\tau_i = v_i/|-\Sigma_j m_j \Pi_{ij} \nabla_i W_{ij}|$ computed directly from the SPH code (left frame) and the analytic estimate (right frame) are shown. Estimates are computed from Eq. (34) with $k_1 = k_2 = 1$ used as an approximation for (a) and (b), from Eq. (36) with $k_1' = k_2' = 1$ for (c) and (d), and from Eq. (39) with $k_1'' = k_2'' = 1$ for (e) and (f).

artificial viscosities: Eqs. (11), (13), and (16). The Balsara AV best preserves the angular velocity profile.

One might worry that the spurious increase in the internal energy u or entropy variable A due to shear might also occur on as short a timescale as the viscous dissipation. However, dimensional analysis on Eqs. (20) and (21) shows that the spurious increase in u and A occurs on a timescale $\sim \tau c_s^2/(\gamma(\gamma-1)v\,\Delta v)$. In typical systems $v\Delta v \ll c_s^2$, so that the timescale for u or A to change is considerably longer than the viscous dissipation timescale τ. Figure 26 shows the entropy S as a function of time t for various types of AV. Although AVs with more shear viscosity naturally produce more spurious increase in entropy, in all cases the rate of entropy increase is rather small.

7. DISCUSSION AND SUMMARY

7.1. *Particle Diffusion*

Many of our tests focus on spurious diffusion, the motion of SPHparticles introduced as an artifact of the numerical scheme. We have analyzed spurious diffusion by using SPH particles in a box with periodic boundary conditions to model a stationary fluid of infinite

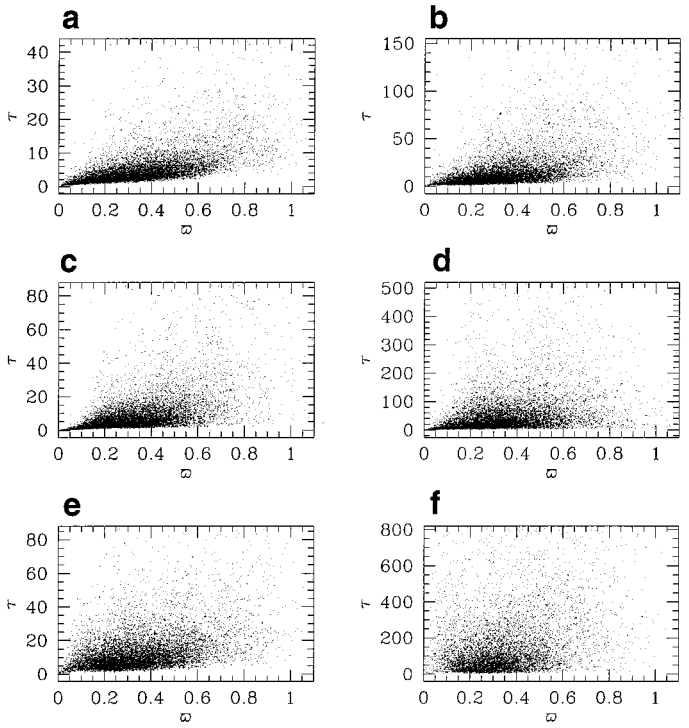

FIG. 24. The timescale $\tau_i = v_i/|-\Sigma_j m_j \Pi_{ij} \nabla_i W_{ij}|$ computed directly from the SPH code for various artificial viscosities after 1 time unit of free evolution. The various AV schemes and parameters α and β are the same as in Fig. 23.

extent. For various noise levels (particle velocity dispersions) and neighbor numbers N_N, we measure the rate of diffusion, which we quantify by calculating a diffusion coefficient D. Although strong shocks and AV in SPH calculations can lead to additional particle mixing [28], particle diffusion is the dominant contribution to spurious mixing in weakly shocked fluids.

Once expressed in terms of the number density of SPH particles and the sound speed, these diffusion coefficients can therefore be used to estimate spurious deviations in particle positions in a wide variety of applications, including self-gravitating systems. For each particle in some large-scale simulation, this spurious deviation is estimated simply from Eq. (28). The coefficient D in the integrand of Eq. (28) depends on the particle's velocity deviation from the local flow, the local number density n of particles, and the local sound speed c_s, so that these quantities need to be monitored for each particle during the calculation. Such a scheme is used in Section 4 to estimate spurious mixing in an equilibrium polytrope and has also been successfully applied in the context of stellar collision simulations [19]. Indeed, the diffusion coefficients provide an extremely valuable means of estimating spurious mixing in real simulations *with artificial viscosity*. For the headon collisions presented in Ref. [19], such estimates were compared with those of a second method which automatically includes the effects of artificial viscosity. For the seven simulations for which a comparison was possible, the two methods gave root mean square displacements that agreed to within a factor of 1.4. The great advantage of using diffusion coefficients is that they can be applied in all cases.

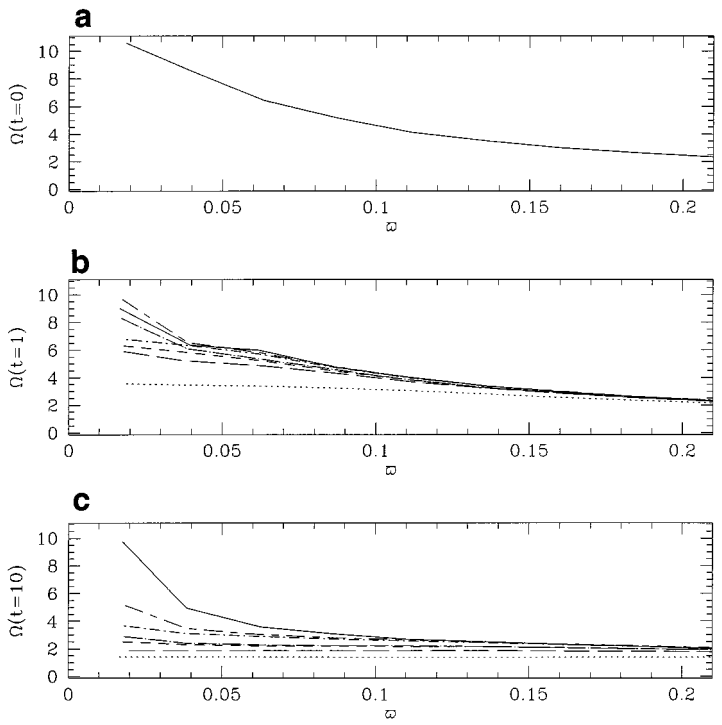

FIG. 25. The angular velocity Ω as a function of cylindrical radius ϖ at times (a) $t = 0$, (b) $t = 1$, and (c) $t = 10$ in seven different calculations which began with the same initial conditions but implemented different artificial viscosities, namely, from top to bottom in (c): no AV (solid curve), $\alpha = 0$ and $\beta = 2 \times \gamma/2$ in Eq. (16) (short dash–long dash), $\alpha = 0$ and $\beta = 2$ in Eq. (13) (dot–short dash), $\alpha = 2 \times \gamma/2$ and $\beta = 0$ in Eq. (16) (dot–long dash), $\alpha = 0$ and $\beta = 2$ in Eq. (11) (short dash), $\alpha = 2$ and $\beta = 0$ in Eq. (13) (long dash), and $\alpha = 2$ and $\beta = 0$ in Eq. (11) (dotted).

For sufficiently low noise levels, the diffusion coefficient essentially vanishes, as the particles simply oscillate around equilibrium lattice sites. We say that such a system has "crystallized." For a neighbor number $N_N \approx 64$, a system of SPH particles will crystallize if the root mean square velocity dispersion is less than about 3–4% of the sound speed. We find that, for the range of N_N that we explored ($32 \leq N_N \leq 64$), crystallized cubic lattices are unstable against perturbations, while lattice types with large packing fractions, such as hexagonal close-packed, are stable. For this reason it may sometimes be better to construct initial data by placing particles in a close-packed lattice, rather than in a cubic lattice as is often done. In practice, initial particle data are typically constructed by first relaxing the system with an artificial drag force, a procedure which automatically produces a stable lattice structure but also spuriously removes small amounts of internal energy.

The diffusion coefficients have been measured using equal mass particles. Sometimes, however, SPH calculations use particles of unequal mass so that less dense regions can still be highly resolved. To test the effects of unequal mass particles in a self-gravitating system, we constructed an equilibrium $n = 1.5$ polytrope, using particle masses which increased with radius in the initial configuration. Allowing the system to evolve, we observed that the heaviest particles gradually migrated towards the center of the star, exchanging places with less massive particles. For a polytrope modeled with $N \approx 1.4 \times 10^4$ particles and a

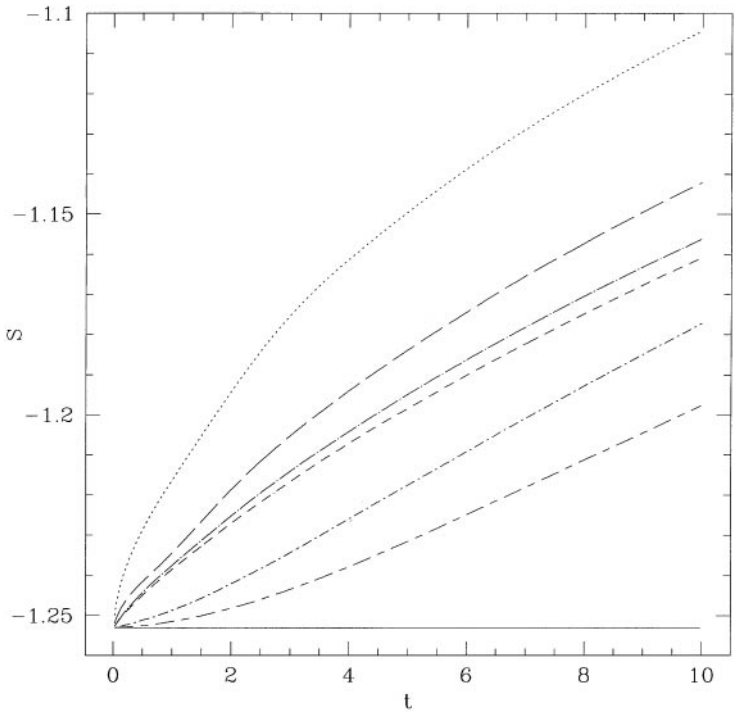

FIG. 26. Entropy S as a function of time for the seven calculations presented in Fig. 25. The various line types are as in Fig. 25.

neighbor number $N_N \approx 64$, the distribution of particle masses is reversed within roughly 80 dynamical timescales. This is caused by the interactions among neighboring particles via the smoothing kernel. These interactions allow energy exchange, and equipartition of energy then requires the heavier particles to sink into the gravitational potential well. Spurious mixing is therefore a more complicated process in calculations which use unequal mass particles: each particle has a preferred direction to migrate, and in a dynamical application this direction can be continually changing. For simulations in which fluid mixing is important and density contrasts are not extreme, equal mass particles are an appropriate choice.

7.2. *Shock Tube Tests*

The diffusion tests just described are all done in the absence of shocks and without AV. To test the AV schemes described in Section 2, we turn to a periodic version of the 1D Riemann shock-tube problem of Sod [56]. Initially, fluid slabs with constant (and alternating) density ρ and pressure p are separated by an infinite number of planar, parallel, and equally spaced interfaces. We treat this inherently 1D problem with both a 1D and a 3D SPH code. The 1D code is naturally more accurate and provides a benchmark against which we can compare the results of our 3D code. In both cases, periodic boundary conditions allow us to model the infinite number of slabs.

Using various values of α and β, we performed a number of such shock-tube calculations with our 3D code, at both Mach numbers $\mathcal{M} \approx 1.6$ and $\mathcal{M} \approx 13.2$ for $\gamma = 5/3$. In addition, we performed tests with $\gamma = 3$ and $\mathcal{M} \approx 13.2$. For each 3D calculation, we compare the time variation of the internal energy and entropy of the system against that of the 1D calculation.

Furthermore, since any motion perpendicular to the bulk fluid flow is spurious, we were also able to examine spurious mixing. We find that all three forms of AV can handle shocks well. For example, with $N = 10^4$ and $N_N \approx 64$, there is better than 2% agreement with the 1D code's internal energy vs time curve when $\mathcal{M} \approx 1.6$, and agreement at about the 3% level when $\mathcal{M} \approx 13.2$. We also find that both Eqs. (11) and (16), as compared to Eq. (13), allow less spurious mixing and do somewhat better at reproducing the 1D code's results. For all three forms of AV, increasing the strength of the AV allows for less spurious diffusion.

From Tables I–IV, which present results for numerous shock-tube tests, we see that the level at which energy conservation is satisfied depends only weakly on the AV parameters but strongly on the length of the timesteps. Energy is typically conserved to better than 0.1% in the $\gamma = 5/3$ 3D calculations whenever the number of timesteps to reach $t = 4$ exceeded 1000. Monaghan's timestep routine is more efficient, in part because it takes shorter timesteps when shocks are strong (that is, when there are large velocity differences between neighboring particles). The agreement between the 3D and 1D calculations for the internal energy U and entropy S was strongly dependent on the AV parameters α and β (see Subsection 7.4), but only weakly dependent on the Courant number C_N or timestep routine.

Such calculations are a useful and realistic way to calibrate spurious transport, since the test problem, which includes shocks and significant fluid motion, has many of the same properties as real astrophysical problems. In fact, the recoil shocks in stellar collisions do tend to be nearly planar, so that even the 1D geometry of the shock fronts is realistic. The periodic boundary conditions play the role of gravity in the sense that they prevent the gas from expanding to infinity.

7.3. *Shear Flows*

To test the various AV forms in the presence of a shear flow, we impose so-called slipping boundary conditions on a periodic box, as is commonly done in molecular dynamics (see, e.g., [58]). The resulting "stationary Couette flow" has a velocity field close to $(v_x, v_y, v_z) = (v_0 y/L, 0, 0)$ and allows us to measure the numerical viscosity of the particles. As in the shock-tube tests, we also examine spurious mixing in the direction perpendicular to the fluid flow. These shear tests therefore allow us to further investigate the accuracy of our SPH code as a function of the AV parameters and scheme. We find that both the Hernquist and Katz AV (Eq. (13)) and the Balsara AV (Eq. (16)) exhibit less viscosity than the classical AV (Eq. (11)). While the HK AV produces the smallest numerical viscosity for these pure shear flows, it also has the largest spurious diffusion coefficient (see Table IV). The product ηD is smallest for the HK AV, indicating that this form is well suited for keeping spurious mixing at a manageable level during calculations involving shear flows. For all three forms of the AV, increasing α and β tends to damp out the noise and consequently decrease spurious mixing, but it also increases the spurious shear viscosity.

Rotation plays an important role in many hydrodynamic processes. For instance, a collision between stars can yield a rapidly and differentially rotating merger remnant. Even in the absence of shocks, AV tends to damp away differential rotation due to the relative velocity of neighboring particles at slightly different radii, and an initially differentially rotating system will tend towards rigid rotation on the viscous dissipation timescale. In systems best modeled with a perfect fluid, ideally with a viscous timescale $\tau = \infty$, any such angular momentum transport introduced by the SPH scheme is spurious.

As a concrete example, we consider an axisymmetric equilibrium configuration differentially rotating with an angular velocity profile $\Omega(\varpi) \propto \varpi^{-\lambda}$, where ϖ is the distance from the rotation axis and λ is a constant of order unity. We then analytically estimate the viscous dissipation timescale for each of the three AVs discussed in Section 2. These analytic estimates are found to closely match numerically measured values of the timescale. Both the Hernquist and Katz AV (Eq. (13)) and the Balsara AV (Eq. (16)) yield longer viscous timescales than the classical AV (Eq. (11)), and hence are better at maintaining the angular velocity profile. The Balsara AV does best in this regard.

7.4. *Artificial Viscosity Forms and Parameters*

When choosing values of AV parameters, one must weigh the relative importance of shocks, shear, and fluid mixing. For this reason, it is an application-dependent, somewhat subjective matter to specify "optimal values" of α and β. Here, however, we roughly delineate the boundaries of the region in parameter space that gives acceptable results.

Our shock-tube tests of Section 5 are all done with periodic cells each containing mass $M = 0.625$. We find that the quantity $(\Delta(U/E)_{\max})^2 + ((\gamma-1)\Delta S_{\max}/M)^2$ is a convenient measure of how well a calculation matches the 1D code's results for both internal energy and entropy (note that $(\gamma-1)\Delta S_{\max}/M \sim \Delta A_{\max}/A$ for small $\Delta S_{\max}$). Values of $\Delta(U/E)_{\max}$ and $\Delta S_{\max}$ are listed in Tables I–IV.

Examination of the final three columns in Table I leads us to the following acceptable ranges for α in our $\gamma = 5/3$ low Mach number shock-tube tests: $0.2 \lesssim \alpha \lesssim 1$ for the classical AV, $0.1 \lesssim \alpha \lesssim 0.5$ for the HK AV, and $0.2 \lesssim 2\alpha/\gamma \lesssim 1$ for the Balsara AV. If spurious diffusion is not a concern, these ranges for α can all be extended down to a lower limit of $\alpha = 0$. For a given value of α, the acceptable range of β is approximately given by $0.8 \lesssim 2\alpha + \beta \lesssim 3.3$ for the classical AV, and $0.6 \lesssim 2\alpha + \beta \lesssim 1.3$ for the HK AV, and $0.8 \lesssim (2\alpha + \beta)2/\gamma \lesssim 3.3$ for the Balsara AV. For parameters in these ranges, all three AVs handle the low Mach number shocks with roughly the same level of accuracy. When Monaghan's timestep routine is used with $C_N = 0.3$, values of α and β which worked particularly well in our low Mach calculations included $\alpha = 0.2$, $\beta = 1$ for the classical AV, $\alpha = 0.3$, $\beta = 0.5$ for the HK AV, and $\alpha = 0.5 \times \gamma/2$, $\beta = \gamma/2$ for the Balsara AV.

For our high Mach number tests, inspection of Tables III and IV leads to the following acceptable ranges for the AV parameters: $1.3 \lesssim \alpha + \beta \lesssim 3.5$ for the classical AV, $1 \lesssim \alpha + \beta \lesssim 1.6$ for the HK AV, and $1.9 \lesssim (\alpha + \beta)2/\gamma \lesssim 4$ for the Balsara AV. The Balsara AV seems capable of handling these high Mach number shocks marginally better than the classical AV, and both are more accurate than the HK AV. Values of α and β which worked particularly well in both of our $\gamma = 5/3$ and $\gamma = 3$ high Mach calculations included $\alpha = 1$, $\beta = 1.5$ for the classical AV, and $\alpha = 2 \times \gamma/2$, $\beta = \gamma/2$ for the Balsara AV. With the HK AV, $\alpha = 0.5$, $\beta = 1$ worked quite well for $\gamma = 5/3$, as did $\alpha = 0.5$, $\beta = 0.5$ for $\gamma = 3$. By performing these high Mach calculations for two different values of γ, we have determined that the ranges of acceptable AV parameters are only weakly dependent on the equation of state for both the classical AV and the HK AV. For the Balsara AV, we find that α and β should scale roughly as γ, so that softer equations of state require larger AV parameters.

Our shear tests of Section 6 allow us to further examine the accuracy of our SPH code as a function of the AV parameters. Not surprisingly, increasing the strength of the AV tends to increase the measured viscosity η and decrease the measured spurious diffusion coefficient D. The product of the viscosity and the diffusion coefficient provides a convenient

(but somewhat arbitrary) measure of a calculation's accuracy. We find that increasing α typically tends to increase the product ηD in our shear tests, and we consequently choose as the "optimal" value of α a relatively small value for which the shock-tube tests (both low and high Mach number) give acceptable results.

The combined results of our shock-tube and shear tests therefore suggest a single set of AV parameters which are appropriate in a large number of situations: $\alpha \approx 0.5$, $\beta \approx 1$ for the classical AV, $\alpha \approx \beta \approx 0.5$ for the Hernquist and Katz AV, and $\alpha \approx \beta \approx \gamma/2$ for the Balsara AV. We will refer to these parameters as "optimal"; however, these choices should be modified depending on the particular application. For instance, if spurious mixing is not a concern and if only weak shocks ($\mathcal{M} \lesssim 2$) are expected during a calculation, then a smaller value of α is appropriate. Likewise, if strong shocks are expected ($\mathcal{M} \gtrsim$ a few) and shear viscosity is not a concern, then a stronger AV is justified.

Our recommended values for α and β correspond to a somewhat weaker AV than is typically suggested in the literature (e.g., $\alpha \approx 1$, $\beta \approx 2$ for the classical AV). While larger AV parameters are appropriate in extreme cases ($\mathcal{M} \gtrsim 10$), we feel our suggested values are slightly more accurate for most situations. Furthermore, since errors do not change significantly when the energy rather than the entropy equation is integrated (the only major difference being a larger $\Delta S_{\max}$ for the energy equation, by a roughly constant amount, see Table II), we conclude that these "optimal" parameters are insensitive to the means by which the thermodynamics is treated. However, we have not tested the dependence of the optimal AV parameters on the neighbor number N_N in detail, nor have we performed test calculations in which both shear flows and shocks are *simultaneously* occurring.

Morris and Monaghan [30] have recently tested the classical AV of Eq. (12) with a *time-varying* viscosity parameter α, and with $\beta = 2\alpha$. The evolution of α is determined for each particle by a source and decay equation, causing the AV to be significantly active only in the immediate vicinity of a shock. The results of their tests are encouraging, and their idea of time-varying AV coefficients could be applied to any AV form.

Our results concerning the various AV forms can be summarized as follows. We find that the AVs defined by Eqs. (11) and (16) do equally well both in their handling of shocks and in their controlling of spurious mixing, and do slightly better than Eq. (13). Furthermore, both Eqs. (13) and (16) do introduce less numerical viscosity than Eq. (11). Since use of Eq. (16), Balsara's form of AV, does indeed significantly decrease the amount of shear viscosity without sacrificing accuracy in the treatment of shocks, we conclude that it is an appropriate choice for a broad range of problems. This is consistent with the successful use of Balsara's AV reported by Navarro and Steinmetz [59] in their models of rotating galaxies.

Balsara's viscosity was constructed to be quite similar to the classical AV in form; the main difference is that Balsara's form contains a "switch" which suppresses the AV in regions of large vorticity. It is a simple matter to generate more sensitive switches than the one in Eq. (16). For instance, instead of $(f_i + f_j)/2$ one could use $f_i f_j$ (or more generally $(f_i f_j)^k$, with $k \gtrsim 1$). Alternatively, in place of the form function f_i defined by Eq. (18), one could use

$$g_i = \frac{\left(\boldsymbol{\nabla} \cdot \mathbf{v}\right)_i^2}{\left(\boldsymbol{\nabla} \cdot \mathbf{v}\right)_i^2 + \left(\boldsymbol{\nabla} \times \mathbf{v}\right)_i^2 + \eta' c_i^2 / h_i^2}. \tag{40}$$

As expected from scaling analyses such as in Subsection 6.2, the viscous dissipation

timescale can be increased by adopting more sensitive switches such as these. However, such switches also tend to allow a faster rate of spurious particle diffusion. We have performed a handful of tests which suggest that such generalizations of Balsara's AV may also handle shocks well, although more tests are necessary.

ACKNOWLEDGMENTS

J.C.L. is supported in part by NSF AST 93-15375 and by a New York Space Grant Fellowship. A.S. is supported in part by the Natural Sciences and Engineering Research Council of Canada. F.A.R. is supported in part by NSF Grant AST-9618116 and by a Sloan Research Fellowship. S.L.S. is supported in part by NSF Grant AST 96-18524 and NASA Grant NAG5-7152 at the University of Illinois at Urbana-Champaign. Some computations were performed at the Cornell Theory Center. This work was also partially supported by the National Computational Science Alliance under Grant AST970022N and utilized the NCSA SGI/CRAY POWER CHALLENGEarray and the NCSA SGI/CRAY Origin2000.

REFERENCES

1. R. W. Hockney and J. W. Eastwood, *Computer Simulations Using Particles* (Hilger, Bristol, 1988).
2. D. H. Porter and P. R. Woodward, High-resolution simulations of compressible convection using the piecewise-parabolic method, *Astrophys. J. Supp.* **93**, 309 (1994).
3. L. B. Lucy, A numerical approach to the testing of the fission hypothesis, *Astron. J.* **82**, 1013 (1977).
4. R. A. Gingold and J. J. Monaghan, Smoothed particle hydrodynamics—Theory and application to non-spherical stars, *Mon. Not. R. Astron. Soc.* **181**, 375 (1977).
5. J. J. Monaghan, Smoothed particle hydrodynamics, *Annu. Rev. Astron. Astrophys.* **30**, 543 (1992).
6. F. A. Rasio and J. C. Lombardi, Smoothed particle hydrodynamics calculations of stellar interactions, *J. Comput. Appl. Math.*, in press.
7. J. J. Monaghan and J. C. Lattanzio, A simulation of the collapse and fragmentation of cooling molecular clouds, *Astrophys. J.* **375**, 177 (1991).
8. A. Burket, M. R. Bate, and P. Boddenheimer, Protostellar fragmentation in a power-law density distribution, *Mon. Not. R. Astron. Soc.* **289**, 497 (1997).
9. A. F. Nelson, W. Benz, F. C. Adams, and D. Arnett, Dynamics of circumstellar disks, *Astrophys. J.* **502**, 342 (1998).
10. A. P. Boss, A. G. W. Cameron, and W. Benz, *Icarus* **97**, 134 (1992).
11. M. Herant and W. Benz, Postexplosion hydrodynamics of SN 1987A, *Astrophys. J.* **387**, 294 (1992).
12. D. Garcia-Senz, E. Bravo, and N. Serichol, A particle code for deflagrations in white dwarfs. I. Numerical techniques, *Astrophys. J. Supp.* **115**, 119 (1998).
13. P. Laguna, W. A. Miller, W. H. Zurek, and M. B. Davies, Tidal disruptions by supermassive black holes—Hydrodynamic evolution of stars on a Schwarzschild background, *Astophys. J. Lett.* **410**, L83 (1993).
14. N. Katz, D. H. Weinberg, and L. Hernquist, Cosmological simulations with TreeSPH, *Astrophys. J. Supp.* **105**, 19 (1996).
15. P. R. Shapiro, H. Martel, J. V. Villumsen, and J. M. Owen, Adaptive smoothed particle hydrodynamics, with application to cosmology: Methodology, *Astrophys. J. Supp.* **103**, 269 (1996).
16. N. Katz, Dissipational galaxy formation. II. Effects of star formation, *Astrophys. J.* **391**, 502 (1992).
17. M. Steinmetz, GRAPESPH: Cosmological smoothed particle hydrodynamics simulations with the special-purpose hardware GRAPE, *Mon. Not. R. Astron. Soc.* **278**, 1005 (1996).
18. J. C. Lombardi, F. A. Rasio, and S. L. Shapiro, On blue straggler formation by direct collisions of main sequence stars, *Astrophys. J. Lett.* **445**, L117 (1995).
19. J. C. Lombardi, F. A. Rasio, and S. L. Shapiro, Collisions of main-sequence stars and the formation of blue stragglers in globular clusters, *Astrophys. J.* **468**, 797 (1996).

20. F. A. Rasio and S. L. Shapiro, Hydrodynamical evolution of coalescing binary neutron stars, *Astrophys. J.* **401**, 226 (1992).
21. F. A. Rasio and S. L. Shapiro, Hydrodynamics of binary coalescence. 2. Polytropes with $\Gamma = 5/3$, *Astrophys. J.* **438**, 887 (1995).
22. M. B. Davies, W. Benz, T. Piran, and F. K. Thielemann, Merging neutron stars. 1. Initial results for coalescence of noncorotating systems, *Astrophys. J.* **431**, 742 (1994).
23. J. M. Centrella and S. L. W. McMillan, Gravitational radiation from nonaxisymmetric collisions of neutron stars, *Astrophys. J.* **416**, 719 (1993).
24. X. Zhuge, J. M. Centrella, and S. L. W. McMillan, Gravitational radiation from coalescing binary neutron stars, *Phys. Rev. D* **50**, 6247 (1994).
25. X. Zhuge, J. M. Centrella, and S. L. W. McMillan, Gravitational radiation from the coalescence of binary neutron stars: Effects due to the equation of state, spin, and mass ratio, *Phys. Rev. D* **54**, 7261 (1996).
26. R. A. Gingold and J. J. Monaghan, On the fragmentation of differentially rotating clouds, *Mon. Not. R. Astron. Soc.* **204**, 715 (1983).
27. L. Hernquist and N. Katz, TREESPH—A unification of SPH with the hierarchical tree method, *Astrophys. J. Supp.* **70**, 419 (1989).
28. J. J. Monaghan, *J. Comput. Phys.* **82**, 1 (1989).
29. D. Balsara, Von Neumann stability analysis of smoothed particle hydrodynamics—Suggestions for optimal algorithms, *J. Comput. Phys.* **121**, 357 (1995).
30. J. P. Morris and J. J. Monaghan, A switch to reduce SPH viscosity, *J. Comput. Phys.* **136**, 41 (1997).
31. A. E. Evrard, Beyond N-body—3D cosmological gas dynamics, *Mon. Not. R. Astron. Soc.* **235**, 911 (1988).
32. L. Hernquist, Performance characteristics of tree codes, *Astrophys. J. Supp.* **64**, 715 (1987).
33. W. Benz, R. L. Bowers, A. G. W. Cameron, and W. H. Press, Dynamic mass exchange in doubly degenerate binaries. I. 0.9 and 1.2 solar mass stars, *Astrophys. J.* **348**, 647 (1990).
34. W. Benz and J. G. Hills, Three-dimensional hydrodynamical simulations of stellar collisions. I. Equal-mass main-sequence stars, *Astrophys. J.* **323**, 614 (1987).
35. A. Sills, J. C. Lombardi, C. D. Bailyn, P. Demarque, F. A. Rasio, and S. L. Shapiro, Evolution of stellar collision products in globular clusters. I. Head-on collisions, *Astrophys. J.* **487**, 290 (1997).
36. M. Steinmetz and E. Müller, On the capabilities and limits of smoothed particle hydrodynamics, *Astron. Astrophys.* **268**, 391 (1993).
37. M. B. Davies, M. Ruffert, W. Benz, and E. Müller, A comparison between SPH and PPM: Simulations of stellar collisions, *Astron. Astrophys.* **272**, 430 (1993).
38. H. Kang *et al.*, A Comparison of cosmological hydrodynamic codes, *Astrophys. J.* **430**, 83 (1994).
39. S. C. Smith, J. L. Houser, and J. M. Centrella, Simulations of nonaxisymmetric instability in a rotating star: A comparison between Eulerian and smooth particle hydrodynamics, *Astrophys. J.* **458**, 236 (1996).
40. M. Ruffert, M. Rampp, and H.-Th. Janka, Coalescing neutron stars—Gravitational waves from polytropic models, *Astron. Astrophys.* **32**1, 991 (1997).
41. J. J. Monaghan and J. C. Lattanzio, A refined particle method for astrophysical problems, *Astron. Astrophys.* **149**, 135 (1985).
42. W. Benz, W. L. Slattery, and A. G. W. Cameron, The origin of the moon and the single-impact hypothesis, I, *Icarus* **66**, 515 (1986).
43. J. J. Monaghan, *Comput. Phys. Rep.* **3**, 71 (1985).
44. R. Klessen, GRAPESPH with fully periodic boundary conditions: Fragmentation of molecular clouds, *Mon. Not. R. Astron. Soc.* **292**, 11 (1997).
45. H. M. P. Couchman, P. A. Thomas, and F. R. Pearce, Hydra: An adaptive-mesh implementation of P3M-SPH, *Astrophys. J.* **452**, 797 (1995).
46. R. Dave, J. Dubinski, and L. Hernquist, Parallel treeSPH, *New Astron.* **2**, 277 (1997).
47. G. Efstathiou, M. Davis, S. D. M. White, and C. S. Frenk, Numerical techniques for large cosmological N-body simulations, *Astrophys. J. Supp.* **57**, 241 (1985).
48. F. A. Rasio, *Hydrodynamical Calculations of Stellar Interactions*, Ph.D. Thesis, Cornell University, 1991.

49. N. H. Wells *et al.*, *Comput. Phys.* **4**, 507 (1990).
50. L. Hernquist, Some cautionary remarks about smoothed particle hydrodynamics, *Astrophys. J.* **404**, 717 (1993).
51. R. P. Nelson and J. C. B. Papaloizou, Three-dimensional hydrodynamic simulations of collapsing prolate clouds, *Mon. Not. R. Astron. Soc.* **265**, 905 (1993).
52. R. P. Nelson and J. C. B. Papaloizou, Variable smoothing lengths and energy conservation in smoothed particle hydrodynamics, *Mon. Not. R. Astron. Soc.* **270**, 1 (1994).
53. A. Serna, J.-M. Alimi, and J.-P. Chièze, Adaptive smooth particle hydrodynamics and particle-particle coupled codes: Energy and entropy conservation, *Astrophys. J.* **461**, 884 (1996).
54. F. A. Rasio and S. L. Shapiro, Collisions of giant stars with compact objects—Hydrodynamical calculations, *Astrophys. J.* **377**, 559 (1991).
55. M. P. Allen and D. J. Tildesley, *Computer Simulations of Liquids* (Oxford Univ. Press, New York, 1989).
56. G. A. Sod, *J. Comput. Phys.* **27**, 1 (1978).
57. R. Courant and K. O. Friedrichs, *Supersonic Flow and Shock Waves* (Springer-Verlag, New York, 1976).
58. T. Naitoh and S. Ono, The shear viscosity of hard-sphere fluid via non-equilibrium molecular dynamics, *Phys. Lett. A* **57**, 448 (1976).
59. J. F. Navarro and M. Steinmetz, The effects of a photoionizing ultraviolet background on the formation of disk galaxies, *Astrophys. J.* **478**, 13 (1997).